Journal of Computational Physics 401 (2020) 109050

Contents lists available at ScienceDirect

Journal of Computational Physics

www.elsevier.com/locate/jcp

A quasi-optimal non-overlapping domain decomposition method for two-dimensional time-harmonic elastic wave problems

V. Mattesi [a,*], M. Darbas [b], C. Geuzaine [a]

[a] Department of Electrical Engineering and Computer Science, University of Liège, Belgium
[b] LAMFA, University of Picardie Jules Verne, Amiens, France

ARTICLE INFO

Article history:
Received 7 June 2019
Received in revised form 14 October 2019
Accepted 15 October 2019
Available online 22 October 2019

Keywords:
Domain decomposition method
Non-overlapping Schwarz method
Scattering
2D time-harmonic elastic waves
High-frequency

ABSTRACT

This article presents the construction of a new non-overlapping domain decomposition method (DDM) for two-dimensional elastic scattering problems. The method relies on a high-order Transmission Boundary Condition (TBC) between sub-domains, which accurately approximates the exact Dirichlet-to-Neumann map. First, we explain the derivation of this new TBC in the context of a non-overlapping DDM. Next, a mode-by-mode convergence study for a model problem is presented, which shows the new method to be quasi-optimal, i.e. with an optimal convergence rate for evanescent modes and an improved convergence rate for the other modes compared to the standard low-order Lysmer-Kuhlemeyer TBC. Finally, the effectiveness of the new DDM is demonstrated in a finite element context by analyzing the behavior of the method on high-frequency elastodynamic simulations.

© 2019 Elsevier Inc. All rights reserved.

0. Introduction

The accurate numerical modeling of high-oscillatory elastic phenomena is a timely research field with a large panel of applications, from seismology and non-destructive testing to medical ultrasound. Amongst the various numerical techniques that can be used to solve such problems [33], the Finite Element Method (FEM) is one of the most versatile. Applying the FEM in the frequency domain leads however to the solution of very large, complex and possibly indefinite linear systems. To overcome the limits of direct sparse solvers and/or the possibly slow convergence of Krylov subspace iterative solvers [17] for such problems, we investigate non-overlapping Domain Decomposition Methods (DDM), which allow to work onto sub-problems of smaller sizes. Such methods were first introduced by Lions [26] for the Laplace equation, before being adapted by Després to the Helmholtz equation [13]. The first step of the method consists in partitioning the domain by introducing fictitious boundaries. Then, continuity conditions are imposed onto these artificial interfaces and the problem is solved by iterating over the sub-domains to obtain the final solution on the overall domain. For wave-type problems, the continuity conditions must be Transmission Boundary Conditions (TBC) of Robin type [3], also referred to as impedance or generalized impedance conditions. The subdomain partitioning makes these methods particularly well suited for implementations on parallel computers.

A key point to get an efficient iterative algorithm lies in the derivation of non-expensive and accurate TBCs. The optimal convergence is obtained by using the exact Dirichlet-to-Neumann (DtN) map as transmission conditions. However, the exact DtN operator is a non-local operator and leads to an expensive procedure in practice. For time-harmonic acoustic and

* Corresponding author.
E-mail address: vanessa.mattesi@ulige.be (V. Mattesi).

https://doi.org/10.1016/j.jcp.2019.109050
0021-9991/© 2019 Elsevier Inc. All rights reserved.

electromagnetic waves, various approximations of the DtN have been proposed over the years, giving rise to so-called optimized Schwarz methods (see e.g. [14]). Quasi-optimal local transmission conditions were proposed in [6,5] based on high-order Padé approximations of the DtN operator. For time-harmonic elastic waves however the state-of-the-art in DDM is much younger. The only attempt so far at constructing an optimized Schwarz method can be found in [7], which relies on a local Taylor transmission condition and necessitates an overlap between the subdomains. In addition, this condition only ensures the convergence of the DDM algorithm for non-grazing modes, under a minimal overlap-width constraint. Designing domain decomposition schemes that do not require an overlap between the subdomains is however desirable from a practical point of view, as they lead to smaller subproblems and easier grid management on parallel computers. In this paper, we propose a new square-root based transmission condition for 2D elastodynamics based on the regularized DtN map described in [28,8], that can be used for both overlapping and non-overlapping DDM. We prove with a mode-by-mode convergence study on a model problem that the resulting non-overlapping DDM is quasi-optimal, i.e. with an optimal convergence rate for evanescent modes and an improved convergence rate for the other modes compared to the standard low-order Lysmer-Kuhlemeyer TBC [27]. We then present a Padé-localized version of this TBC and its implementation in a Finite Element context, and discuss the performance of the new algorithm on numerical examples.

The paper is organized as follows. After describing the Navier problem and the non-overlapping DDM in Section 1, we introduce the new high-order transmission boundary condition in Section 2. In Section 3, we analyze the convergence of the resulting DDM for a model problem and prove its quasi-optimality. Section 4 is devoted to the localization procedure of the transmission operator and Section 5 to the implementation with finite elements. Finally, we discuss the pros and cons of the new TBC around several 2D numerical results which validate the conclusions of the modal analysis from Section 3.

1. Navier exterior problem and non-overlapping domain decomposition method

Let us consider a two-dimensional time-harmonic scattering problem of an incident elastic wave by an impenetrable body Ω^- with a closed boundary $\Gamma := \partial\Omega^-$ of class $\mathcal{C}^2$ at least. Let Ω^+ denote the associated exterior domain $\mathbb{R}^2\backslash\overline{\Omega^-}$. We are interested in finding the scattered field $\boldsymbol{u}^+$ solution to the exterior Navier equation with a Dirichlet boundary condition and satisfying the Kupradze radiation conditions [25] at infinity

$$\begin{cases} \operatorname{div}\sigma(\boldsymbol{u}^+) + \rho\omega^2\boldsymbol{u}^+ = 0 \quad \text{in } \Omega^+, \\ \boldsymbol{u}^+_{|\Gamma} = -\boldsymbol{u}^{\text{inc}}_{|\Gamma} \quad \text{on } \Gamma, \\ \lim\limits_{r\to\infty} \sqrt{r}\left(\dfrac{\partial\psi_{\{p,s\}}}{\partial r} - i\kappa_{\{p,s\}}\psi_{\{p,s\}}\right) = 0, \quad r = |\boldsymbol{x}|, \end{cases} \tag{1}$$

with $\boldsymbol{u}^{\text{inc}}$ an incident wave field which is assumed to solve the Navier equation in the absence of any scatterer. The Lamé parameters, μ and λ, the angular frequency ω and the density ρ are positive constants. In the case of 2D isotropic elastodynamics, the stress and strain tensors are given by $\sigma(\boldsymbol{u}^+) = \lambda(\operatorname{div}\boldsymbol{u}^+)\mathrm{I}_2 + 2\mu\varepsilon(\boldsymbol{u}^+)$ and $\varepsilon(\boldsymbol{u}^+) = \frac{1}{2}\left([\nabla\boldsymbol{u}^+] + [\nabla\boldsymbol{u}^+]^t\right)$ respectively, where I_2 is the 2-by-2 identity matrix and $[\nabla\boldsymbol{u}^+]$ is the matrix whose j-th column is the gradient of the j-th component of $\boldsymbol{u}^+$. The displacement field $\boldsymbol{u}^+$ is decomposed into the longitudinal field $\boldsymbol{u}_p = \nabla\psi_p$ and the transverse field $\boldsymbol{u}_s = \boldsymbol{u}^+ - \boldsymbol{u}_p = \mathbf{curl}\,\psi_s$, where the Lamé potentials ψ_p and ψ_s satisfy

$$\begin{cases} \psi_p = -\kappa_p^{-2}\operatorname{div}\boldsymbol{u}^+ \\ \Delta\psi_p + \kappa_p^2\psi_p = 0 \end{cases} \quad \text{and} \quad \begin{cases} \psi_s = \kappa_s^{-2}\operatorname{curl}\boldsymbol{u}^+ \\ \Delta\psi_s + \kappa_s^2\psi_s = 0 \end{cases} \tag{2}$$

with respective P- and S-wavenumbers $\kappa_p^2 = \rho\omega^2/(\lambda+2\mu)$ and $\kappa_s^2 = \rho\omega^2/\mu$. Notice that in two dimensions, the vector rotational operator is defined for a scalar function φ by $\mathbf{curl}\,\varphi = (\partial_y\varphi, -\partial_x\varphi)^t$, whereas the scalar rotational operator acting on a vector field $\mathbf{v} = (v_x, v_y)^t$ is given by $\operatorname{curl}\mathbf{v} = \partial_x v_y - \partial_y v_x$. The wavelengths are defined by $\lambda_{\{p,s\}} = 2\pi/\kappa_{\{p,s\}}$.

To numerically compute the solution to problem (1), we combine Absorbing Boundary Conditions (ABCs) with an optimized Schwarz domain decomposition method. The infinite propagation domain Ω^+ is truncated with a fictitious boundary Γ^∞ enclosing the obstacle. Let us denote by Ω the bounded domain delimited by Γ and Γ^∞; and by $\boldsymbol{n} = (n_x, n_y)^t$ the outer unit normal vector to the boundary Γ^∞. The Absorbing Boundary Condition introduced on Γ^∞ simulates the radiation condition and the resulting bounded boundary-value problem is the following: find $\boldsymbol{u}$ solution to

$$\begin{cases} \operatorname{div}\sigma(\boldsymbol{u}) + \rho\omega^2\boldsymbol{u} = 0, & \text{in } \Omega, \\ \boldsymbol{u}_{|\Gamma} = -\boldsymbol{u}^{\text{inc}}_{|\Gamma}, & \text{on } \Gamma, \\ \boldsymbol{t}_{|\Gamma^\infty} = \mathcal{B}\boldsymbol{u}_{|\Gamma^\infty}, & \text{on } \Gamma^\infty. \end{cases} \tag{3}$$

The Neumann trace, defined by $\boldsymbol{t}_{|\Gamma^\infty} := \sigma\boldsymbol{n} =: \mathcal{T}_{\boldsymbol{n}}\boldsymbol{u}$, is given by the traction operator

$$\mathcal{T}_{\mathbf{n}} = 2\mu\frac{\partial}{\partial\boldsymbol{n}} + \lambda\boldsymbol{n}\operatorname{div} + \mu\,\boldsymbol{n}\times\operatorname{curl}, \tag{4}$$

where $\boldsymbol{n}\times\varphi = (\varphi n_y, -\varphi n_x)^t$ for a given scalar function φ. Using Perfectly Matched Layers (PMLs) [4,10] is another standard technique to truncate the propagation domain and all what follows can be adapted to that case.

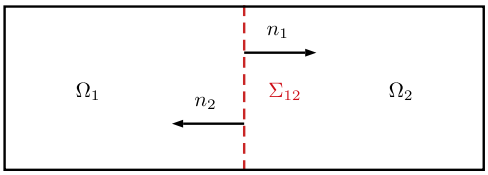


Fig. 1. Example of partition of the domain Ω.

Let us focus on the algorithm of optimized Schwarz Domain Decomposition Method (DDM) [13,26] without overlap for the bounded boundary-value problem (3). The first step of the non-overlapping DDM is to make a partition of the domain Ω with N_{dom} sub-domains Ω_i, $i = 1, \cdots, N_{\text{dom}}$, see Fig. 1. Thus, the sub-domains satisfy $\bar{\Omega} = \cup_{i=1}^{N_{\text{dom}}} \bar{\Omega}_i$ and $\Omega_i \cap \Omega_j = \emptyset$ for all $i \neq j$, $i, j = 1, \cdots, N_{\text{dom}}$. For neighboring sub-domains Ω_i and Ω_j, we denote $\Sigma_{ij} := \bar{\Omega}_i \cap \bar{\Omega}_j$ their interface. Problem (3) can be rewritten as follows on the sub-domains Ω_i, $i = 1, \cdots, N_{\text{dom}}$

$$\begin{cases} \operatorname{div} \sigma(\boldsymbol{u}_i) + \rho\omega^2 \boldsymbol{u}_i = 0, & \text{in } \Omega_i, \\ \boldsymbol{u}_i = -\boldsymbol{u}_i^{\text{inc}}, & \text{on } \Gamma_i, \\ \mathcal{T}\boldsymbol{u}_i = \mathcal{B}\boldsymbol{u}_i, & \text{on } \Gamma_i^{\infty}, \end{cases} \tag{5}$$

supplemented with the following continuity conditions on the interface between neighboring subdomains Ω_i and Ω_j

$$\begin{cases} \boldsymbol{u}_i & = \boldsymbol{u}_j & \text{on } \Sigma_{ij}, \\ \mathcal{T}_{\boldsymbol{n}_i}\boldsymbol{u}_i & = -\mathcal{T}_{\boldsymbol{n}_j}\boldsymbol{u}_j & \text{on } \Sigma_{ij}. \end{cases} \tag{6}$$

Following the method introduced by Lions [26] in the context of the Laplace equation and adapted to wave propagation problems by Després [13], the second step consists in combining the continuity conditions (6) into transmission conditions between neighboring sub-domains and iteratively solving (volume) sub-problems Vol_i on each Ω_i: at iteration $p+1$, find $\boldsymbol{u}_i^{(p+1)} := \boldsymbol{u}_{|\Omega_i}^{(p+1)}$, $i = 1, \cdots, N_{\text{dom}}$ solution to

$$\begin{cases} \operatorname{div} \sigma(\boldsymbol{u}_i^{(p+1)}) + \rho\omega^2 \boldsymbol{u}_i^{(p+1)} = 0, & \text{in } \Omega_i, \\ \boldsymbol{u}_i^{(p+1)} = -\boldsymbol{u}_i^{\text{inc}}, & \text{on } \Gamma_i, \\ \mathcal{T}\boldsymbol{u}_i^{(p+1)} = \mathcal{B}\boldsymbol{u}_i^{(p+1)}, & \text{on } \Gamma_i^{\infty}, \\ \mathcal{T}_{\boldsymbol{n}_i}\boldsymbol{u}_i^{(p+1)} - \mathcal{S}_{\boldsymbol{n}_i}\boldsymbol{u}_i^{(p+1)} = \boldsymbol{g}_{ij}^{(p)}, & \text{on } \Sigma_{ij}, \end{cases} \tag{7}$$

and then in updating the (surface) fields $\boldsymbol{g}_{ji}^{(p+1)}$ by solving the surface systems Sur_{ij}

$$\boldsymbol{g}_{ji}^{(p+1)} = -\boldsymbol{g}_{ij}^{(p)} - (\mathcal{S}_{\boldsymbol{n}_i} + \mathcal{S}_{\boldsymbol{n}_j})\boldsymbol{u}_i^{(p+1)}, \quad \text{on } \Sigma_{ij}. \tag{8}$$

We denoted $\boldsymbol{n}_i$ (resp. $\boldsymbol{n}_j$) the outgoing normal to Ω_i (resp. Ω_j), $i = 1, \cdots, N_{\text{dom}}$, $j = 1, \cdots, N_{\text{dom}}$, $\Gamma_i = \partial\Omega_i \cap \Gamma$, $\Gamma_i^{\infty} = \partial\Omega_i \cap \Gamma^{\infty}$ and $\mathcal{S}_{\boldsymbol{n}}$ the transmission operator. Note that by definition Γ_i or Γ_i^{∞} can be empty sets. The notations $\mathcal{T}_{\boldsymbol{n}}$ and $\mathcal{S}_{\boldsymbol{n}}$ suggest a dependence with respect to the normal vector $\boldsymbol{n}$; details will be given in Section 2.

As has already been discussed in [5,6], solving at each iteration $p+1$ all the local transmission problems (7)–(8) is equivalent to finding $\boldsymbol{g}^{(p+1)}$ the set of boundary data $(\boldsymbol{g}_{ij}^{(p+1)})_{1 \leq i,j \leq N_{\text{dom}}}$ solution to

$$\boldsymbol{g}^{(p+1)} = \mathcal{A}\boldsymbol{g}^{(p)} + \mathbf{b}, \tag{9}$$

where $\mathcal{A} : \times_{i,j=1}^{N_{\text{dom}}} (L^2(\Sigma_{ij}))^2 \to \times_{i,j=1}^{N_{\text{dom}}} (L^2(\Sigma_{ij}))^2$ is the iteration operator and $\mathbf{b} := (\mathbf{b}_{|\Sigma_{ij}})_{1 \leq i,j \leq N_{\text{dom}}} \in \times_{i,j=1}^{N_{\text{dom}}} (L^2(\Sigma_{ij}))^2$ is the source term (given in our case by the Dirichlet and the absorbing boundary condition). Therefore, (7)–(8) can be seen as an iteration of the Jacobi method applied to the linear system

$$(I - \mathcal{A})\boldsymbol{g} = \mathbf{b}, \tag{10}$$

where I is the identity operator. A consequence is that any Krylov subspace iterative solver [31] can be used instead of the simple Jacobi iterative process to find the solution.

2. Transmission operators

The operator $\mathcal{S}_{\boldsymbol{n}}$ aims at approximating the exact exterior DtN map $\Lambda^{\text{ex}} : (H^{\frac{1}{2}}(\Sigma_{ij}))^2 \to (H^{-\frac{1}{2}}(\Sigma_{ij}))^2$ defined by

$$\Lambda^{\text{ex}}(\boldsymbol{u}_{|\Sigma_{ij}}) = \boldsymbol{t}_{|\Sigma_{ij}}. \tag{11}$$

It is well-known that the choice of the operator $\mathcal{S}_{\mathbf{n}}$ directly impacts the convergence of the domain decomposition method [6,5]. We propose to compare two approximations of different orders of the DtN map and the corresponding Transmission Boundary Conditions (TBC).

2.1. Low-order transmission operator

We consider the following low-order approximation of the exact DtN map Λ^{ex}

$$\mathcal{S}^0_{\boldsymbol{n}} := i(\lambda+2\mu)\kappa_p \mathrm{I}_{\boldsymbol{n}} + i\mu\kappa_s \mathrm{I}_{\boldsymbol{\tau}}, \tag{12}$$

where $\mathrm{I}_{\boldsymbol{n}} = \boldsymbol{n}\otimes\boldsymbol{n}$ and $\mathrm{I}_{\boldsymbol{\tau}} = \mathrm{I} - \mathrm{I}_{\boldsymbol{n}}$. This choice corresponds to the radiation conditions given in [25] (see Theorem 2.9 page 127) which are equivalent to Kupradze one's given in (1). The zeroth-order approximation (12) plays the same role as the approximate DtN $i\kappa$ (where κ is the wavenumber) associated with the Sommerfeld radiation condition in acoustics. The operator (12) gives the Lysmer-Kuhlemeyer boundary condition [27,23,24]. Such an approximation was also previously used in the framework of nonreflecting boundary conditions when the artificial boundary is a sphere [19].

Noting that $\mathrm{I}_{\{-\boldsymbol{n}\}} = \mathrm{I}_{\boldsymbol{n}}$, the operator $\mathcal{S}^0_{\boldsymbol{n}}$ satisfies $\mathcal{S}^0_{-\boldsymbol{n}} = \mathcal{S}^0_{\boldsymbol{n}} =: \mathcal{S}^0$. The associated last equation of (7) is called the Low-Order Transmission Boundary Condition (LO-TBC) and is given by

$$\mathcal{T}_{\boldsymbol{n}_i}\boldsymbol{u}_i^{(p+1)} - \mathcal{S}^0\boldsymbol{u}_i^{(p+1)} = \boldsymbol{g}_{ij}^{(p)}, \quad \text{on } \Sigma_{ij}. \tag{13}$$

Thus, the field equation (8) reads

$$\boldsymbol{g}_{ji}^{(p+1)} = -\boldsymbol{g}_{ij}^{(p)} - 2\mathcal{S}^0\boldsymbol{u}_i^{(p+1)}, \quad \text{on } \Sigma_{ij}. \tag{14}$$

We will see in Section 3 that the approximation (12) provides a good spectral behavior of the associated iteration operator $(I-\mathcal{A})$ for the first eigenvalues (associated with propagating modes) only. A similar behavior has been observed with the use of the non-overlapping DDM and low-order DtN approximations for the Helmholtz [6] and Maxwell [5] equations. This motivates the investigation of new high-order transmission conditions.

2.2. Non-local high-order transmission operator

Recent works in 3D elastodynamics have proposed accurate approximations of the exact DtN map in the context of the analytical preconditioning technique for boundary integral equations [12,8] and in the context of the On-Surface Radiation Conditions (OSRC) method [8]. In [28], ideas of [8] have been adapted to the 2D case and were used to derive new high-order ABCs for elasticity. For the non-overlapping DDM we study, these previous results lead us to consider the following high-order (non-local) transmission operator

$$\mathcal{S}^{1,\epsilon}_{\boldsymbol{n}} = (I+\Lambda_{2,\epsilon,\boldsymbol{n}})^{-1}\Lambda_{1,\epsilon,\boldsymbol{n}} + 2\mu\mathcal{M}_{\boldsymbol{n}}, \tag{15}$$

with the operators

$$\Lambda_{1,\epsilon,\boldsymbol{n}} = i\rho\omega^2\left[\boldsymbol{n}\frac{1}{\kappa_{p,\epsilon}}\left(\frac{\Delta_\Gamma}{\kappa^2_{p,\epsilon}}+\mathrm{I}\right)^{-1/2}\boldsymbol{n}\cdot\mathrm{I}_{\boldsymbol{n}} + \boldsymbol{\tau}\frac{1}{\kappa_{s,\epsilon}}\left(\frac{\Delta_\Gamma}{\kappa^2_{s,\epsilon}}+\mathrm{I}\right)^{-1/2}\boldsymbol{\tau}\cdot\mathrm{I}_{\boldsymbol{\tau}}\right], \tag{16}$$

$$\Lambda_{2,\epsilon,\boldsymbol{n}} = -i\left[\boldsymbol{\tau}\left(\frac{\partial_s}{\kappa_{s,\epsilon}}\left(\frac{\Delta_\Gamma}{\kappa^2_{s,\epsilon}}+\mathrm{I}\right)^{-1/2}\boldsymbol{n}\cdot\mathrm{I}_{\boldsymbol{n}}\right) - \boldsymbol{n}\left(\frac{\partial_s}{\kappa_{p,\epsilon}}\left(\frac{\Delta_\Gamma}{\kappa^2_{p,\epsilon}}+\mathrm{I}\right)^{-1/2}\boldsymbol{\tau}\cdot\mathrm{I}_{\boldsymbol{\tau}}\right)\right], \tag{17}$$

and $\mathcal{M}_{\boldsymbol{n}}$ the Günter tangential derivative which is given by

$$\mathcal{M}_{\boldsymbol{n}} = \partial_s(\boldsymbol{n}\cdot\mathrm{I}_{\boldsymbol{n}})\boldsymbol{\tau} - \partial_s(\boldsymbol{\tau}\cdot\mathrm{I}_{\boldsymbol{\tau}})\boldsymbol{n}, \tag{18}$$

where $\kappa_{\{p,s\},\epsilon} := \kappa_{\{p,s\}} + i\epsilon_{\{p,s\}}$ are complexified wavenumbers, $\boldsymbol{\tau} = (-n_y, n_x)^t$ is the unit tangential vector, s the associated curvilinear abscissa along Σ_{ij} and ∂_s is the curvilinear derivative. The Laplace-Beltrami operator over Σ_{ij} is defined by $\Delta_\Gamma = \partial_s^2$ and the inverse of the square-root operator $\left(\frac{\Delta_\Gamma}{\kappa^2_{\{p,s\},\epsilon}}+\mathrm{I}\right)^{-1/2}$ is defined through its spectral decomposition [32]. As we work with complex numbers, the principal determination of the square-root with a branch-cut along the negative real axis will be considered. We consider the same values for the damping parameters $\epsilon_{\{p,s\}}$ arising in the complexified wavenumbers $\kappa_{\{p,s\},\epsilon}$ as the ones derived by solving optimization problems for a sufficiently large wavenumber in the spherical case [11,2,16]: $\epsilon_p = 0.39\kappa_p^{1/3}(\mathcal{H}^2)^{1/3}$ and $\epsilon_s = 0.39\kappa_s^{1/3}(\mathcal{H}^2)^{1/3}$ where $\mathcal{H}$ is the curvature of the boundary Σ_{ij}.

Noting that $\partial^2_{\{-s\}} = \partial^2_s$, we have $\Lambda_{1,\epsilon,\{-\boldsymbol{n}\}} = \Lambda_{1,\epsilon,\boldsymbol{n}}$ (we omit the subscript $\boldsymbol{n}$ in the notation of $\Lambda_{1,\epsilon,\boldsymbol{n}}$), $\Lambda_{2,\epsilon,\{-\boldsymbol{n}\}} = -\Lambda_{2,\epsilon,\boldsymbol{n}}$ and $\mathcal{M}_{\{-\boldsymbol{n}\}} = -\mathcal{M}_{\boldsymbol{n}}$. We deduce that the update equation (8) associated with the non-local high-order transmission operator (15) is equivalent to

$$\boldsymbol{g}_{ji}^{(p+1)} = -\boldsymbol{g}_{ij}^{(p)} - \left[(I+\Lambda_{2,\epsilon,\boldsymbol{n}_i})^{-1}\Lambda_{1,\epsilon} + (I-\Lambda_{2,\epsilon,\boldsymbol{n}_i})^{-1}\Lambda_{1,\epsilon}\right]\boldsymbol{u}_i^{(p+1)}, \quad \text{on } \Sigma_{ij}. \tag{19}$$

In addition, the last equation of (7) when considering the non-local high-order transmission operator (15) is called the non-local High-Order Transmission Boundary Condition (HO-TBC)

$$\mathcal{T}_{\boldsymbol{n}_i}\boldsymbol{u}_i^{(p+1)} - \mathcal{S}_{\boldsymbol{n}_i}^{1,\epsilon}\boldsymbol{u}_i^{(p+1)} = \boldsymbol{g}_{ij}^{(p)}, \quad \text{on } \Sigma_{ij}. \tag{20}$$

In Section 4, we will address an efficient local representation of the non-local operator $\mathcal{S}_{\boldsymbol{n}}^{1,\epsilon}$ using complex Padé approximants which can be easily combined with a finite element discretization.

3. Convergence analysis for large modes on a model problem

In order to study the convergence for large modes (i.e. in the high-frequency part of the Fourier spectrum corresponding to evanescent waves) of the proposed DDM with the non-local HO-TBC (20), we analyze a model problem with two subdomains: a disk-shaped bounded sub-domain Ω_1 of radius R and an unbounded complementary domain Ω_0. We denote by $\Gamma := \partial\Omega_1$ the boundary of Ω_1.

The method consists in solving separately at each iteration the following problems

$$\begin{cases} \text{div}\sigma(\boldsymbol{u}_0^{(p+1)}) + \rho\omega^2\boldsymbol{u}_0^{(p+1)} = 0, \quad \text{in } \Omega_0, \\ \boldsymbol{g}_0^{(p)} = \mathcal{T}_{\boldsymbol{n}_0}\boldsymbol{u}_0^{(p+1)} - \mathcal{S}_{\boldsymbol{n}_0}^{1,\epsilon}\boldsymbol{u}_0^{(p+1)} = -\mathcal{T}_{\boldsymbol{n}_1}\boldsymbol{u}_1^{(p)} - \mathcal{S}_{\boldsymbol{n}_0}^{1,\epsilon}\boldsymbol{u}_1^{(p)}, \quad \text{on } \Gamma, \end{cases} \tag{21}$$

with $\boldsymbol{u}_0$ satisfying the Kupradze radiation conditions, and

$$\begin{cases} \text{div}\sigma(\boldsymbol{u}_1^{(p+1)}) + \rho\omega^2\boldsymbol{u}_1^{(p+1)} = 0, \quad \text{in } \Omega_1, \\ \boldsymbol{g}_1^{(p)} = \mathcal{T}_{\boldsymbol{n}_1}\boldsymbol{u}_1^{(p+1)} - \mathcal{S}_{\boldsymbol{n}_1}^{1,\epsilon}\boldsymbol{u}_1^{(p+1)} = -\mathcal{T}_{\boldsymbol{n}_0}\boldsymbol{u}_0^{(p)} - \mathcal{S}_{\boldsymbol{n}_1}^{1,\epsilon}\boldsymbol{u}_0^{(p)}, \quad \text{on } \Gamma. \end{cases} \tag{22}$$

The convergence analysis can be developed by studying the spectral properties of the iteration operator $\mathcal{A}$ (a 4×4 matrix) defined by

$$\mathcal{A} := \begin{pmatrix} \boldsymbol{0}_2 & \mathcal{A}_0 \\ \mathcal{A}_1 & \boldsymbol{0}_2 \end{pmatrix}, \tag{23}$$

with $\mathcal{A}_0$ and $\mathcal{A}_1$ 2×2 matrices satisfying

$$\mathcal{A}_0\boldsymbol{g}_0^{(p)} := -\boldsymbol{g}_0^{(p)} - (\mathcal{S}_{\boldsymbol{n}_0}^{1,\epsilon} + \mathcal{S}_{\boldsymbol{n}_1}^{1,\epsilon})\boldsymbol{u}_0^{(p+1)}, \ \mathcal{A}_1\boldsymbol{g}_1^{(p)} := -\boldsymbol{g}_1^{(p)} - (\mathcal{S}_{\boldsymbol{n}_0}^{1,\epsilon} + \mathcal{S}_{\boldsymbol{n}_1}^{1,\epsilon})\boldsymbol{u}_1^{(p+1)}. \tag{24}$$

We will first derive an explicit mode-by-mode representation of the fields $\boldsymbol{u}_0$, $\boldsymbol{u}_1$ and the operator $\mathcal{S}_{\boldsymbol{n}}^{1,\epsilon}$. Then, using (21) and (22) we will determine the coefficients of the matrices $\mathcal{A}_0$, $\mathcal{A}_1$ and $\mathcal{A}$. Finally, we will study the asymptotic behavior of the eigenvalues and the spectral radius of $\mathcal{A}$. This leads a convergence result of the non-overlapping DDM for large modes.

3.1. Spectral representation of the solutions

Since we have a cylindrical geometry, we determine the solutions $\boldsymbol{u}_0$ and $\boldsymbol{u}_1$ to problems (21) and (22) mode-by-mode by using a Fourier-Hankel series expansion in the cylindrical coordinates system (r,θ). A standard decomposition in elastodynamics consists in splitting $\boldsymbol{u}_\ell$, $\ell = 0, 1$, into an irrotational potential ψ_ℓ^p and a free-divergence potential ψ_ℓ^s [30]

$$\boldsymbol{u}_\ell = \nabla\psi_\ell^p + \mathbf{curl}\,\psi_\ell^s, \quad \text{for } \ell = 0, 1, \tag{25}$$

when considering

$$\psi_\ell^p = \sum_{m=0}^{+\infty}\psi_{\ell,m}^p e^{im\theta}, \quad \psi_\ell^s = \sum_{m=0}^{+\infty}\psi_{\ell,m}^s e^{im\theta}, \quad \ell = 0, 1, \tag{26}$$

with $\psi_{0,m}^{\{p,s\}}$ solving the exterior problems

$$\begin{cases} \dfrac{1}{r}\partial_r(r\partial_r\psi_{0,m}^{\{p,s\}}) + (\kappa_{\{p,s\}}^2 - \dfrac{m^2}{r^2})\psi_{0,m}^{\{p,s\}} = 0, \quad r > \text{R}, \\ \lim\limits_{r\to\infty}\sqrt{r}(\partial_r\psi_{0,m}^{\{p,s\}} - i\kappa_{\{p,s\}}\psi_{0,m}^{\{p,s\}}) = 0, \end{cases} \tag{27}$$

and $\psi_{1,m}^{\{p,s\}}$ solving the interior ones

$$\frac{1}{r}\partial_r(r\partial_r\psi_{1,m}^{\{p,s\}}) + (\kappa_{\{p,s\}}^2 - \frac{m^2}{r^2})\psi_{1,m}^{\{p,s\}} = 0, \quad r \le \text{R}. \tag{28}$$

It follows that [30,34]

$$\psi_{0,m}^{\{p,s\}} = \alpha_{\{p,s\},m}H_m^{(1)}(\kappa_{\{p,s\}}r) \quad \text{and} \quad \psi_{1,m}^{\{p,s\}} = \beta_{\{p,s\},m}J_m(\kappa_{\{p,s\}}r), \tag{29}$$

where $H_m^{(1)}$ and J_m are the Hankel function of the first-kind and the Bessel function of order m respectively. Let us denote (p_ℓ, q_ℓ) the cylindrical components of $\boldsymbol{u}_\ell$ for $\ell = 0, 1$ and for more readability $\sum_m \nu_m = \sum_{m=0}^{+\infty} \nu_m$. Using the Fourier expansion for $\ell = 0, 1$

$$\boldsymbol{u}_\ell := \sum_m \boldsymbol{u}_{\ell,m} e^{im\theta} = (p_\ell, q_\ell)^t := (\sum_m p_{\ell,m} e^{im\theta}, \sum_m q_{\ell,m} e^{im\theta})^t, \tag{30}$$

we deduce from (25)–(29) and the expressions in cylindric coordinates of $\nabla\varphi = (\partial_r\varphi, \frac{\partial_\theta}{r}\varphi)^t$ and $\mathbf{curl}\varphi = (\frac{\partial_\theta}{r}\varphi, -\partial_r\varphi)^t$ that for a mode m at iteration p

$$\begin{cases} p_{0,m}^{(p)} = \alpha_{p,m}^{(p)} \kappa_p H_m^{(1)'}(\kappa_p r) + \dfrac{im}{r} \alpha_{s,m}^{(p)} H_m^{(1)}(\kappa_s r), \\ q_{0,m}^{(p)} = \dfrac{im}{r} \alpha_{p,m}^{(p)} H_m^{(1)}(\kappa_p r) - \alpha_{s,m}^{(p)} \kappa_s H_m^{(1)'}(\kappa_s r), \\ p_{1,m}^{(p)} = \beta_{p,m}^{(p)} \kappa_p J_m'(\kappa_p r) + \dfrac{im}{r} \beta_{s,m}^{(p)} J_m(\kappa_s r), \\ q_{1,m}^{(p)} = \dfrac{im}{r} \beta_{p,m}^{(p)} J_m(\kappa_p r) - \beta_{s,m}^{(p)} \kappa_s J_m'(\kappa_s r). \end{cases} \tag{31}$$

3.2. Spectral representation of the operators

Let us begin with the traction operator $\mathcal{T}_{\boldsymbol{n}_1}$ (4). In the usual cylindric coordinate system (r, θ), the traction operator applied to $\boldsymbol{u}_\ell = (p_\ell, q_\ell)^t$, for $\ell = 0, 1$, is described by

$$\mathcal{T}_{\boldsymbol{n}_1} \boldsymbol{u}_\ell := \begin{pmatrix} (\lambda + 2\mu)\partial_r p_\ell + \lambda \dfrac{\partial_\theta}{\mathrm{R}} q_\ell + \dfrac{\lambda}{\mathrm{R}} p_\ell \\ \mu \partial_r q_\ell + \mu \dfrac{\partial_\theta}{\mathrm{R}} p_\ell - \dfrac{\mu}{\mathrm{R}} q_\ell \end{pmatrix}. \tag{32}$$

Expression (32) comes from $\mathcal{T}_{\boldsymbol{n}} \boldsymbol{u}_\ell = \sigma(\boldsymbol{u}_\ell)\boldsymbol{n} = (\lambda(\mathrm{div}\, \boldsymbol{u}_\ell) I_2 + 2\mu\varepsilon(\boldsymbol{u}_\ell))\boldsymbol{n}$ when taking the divergence in cylindrical coordinates, $\boldsymbol{n} = \boldsymbol{n}_1 = (1, 0)^t$ and by definition of the strain tensor in cylindrical coordinates (see page 124 [18])

$$\varepsilon(\boldsymbol{u}_\ell) := \begin{pmatrix} \partial_r p_\ell & \dfrac{1}{2}\left(\dfrac{1}{r}\partial_\theta p_\ell + \partial_r q_\ell - \dfrac{q_\ell}{r}\right) \\ \dfrac{1}{2}\left(\dfrac{1}{r}\partial_\theta p_\ell + \partial_r q_\ell - \dfrac{q_\ell}{r}\right) & \dfrac{1}{r}\left(\partial_\theta q_\ell + p_\ell\right) \end{pmatrix}. \tag{33}$$

Noting that $\partial_\theta \boldsymbol{u}_\ell = im\boldsymbol{u}_\ell$ (see (30)), we obtain

$$\mathcal{T}_{\boldsymbol{n}_1} \boldsymbol{u}_\ell = \sum_m \mathcal{T}_{\boldsymbol{n}_1,m} \boldsymbol{u}_{\ell,m} e^{im\theta}, \tag{34}$$

with $\mathcal{T}_{\boldsymbol{n}_1,m}$ a 2×2 matrix defined mode-by-mode as

$$\mathcal{T}_{\boldsymbol{n}_1,m} = \begin{pmatrix} \dfrac{\lambda}{\mathrm{R}} + (\lambda + 2\mu)\partial_r \cdot & i\dfrac{\lambda m}{\mathrm{R}} \\ i\dfrac{\mu m}{\mathrm{R}} & -\dfrac{\mu}{\mathrm{R}} + \mu\partial_r \cdot \end{pmatrix}. \tag{35}$$

Similarly, using the relation $\partial_s = \partial_\theta/\mathrm{R}$ on the surface Γ with normal $\boldsymbol{n}_1$ and the expression of the operators (16)–(17)–(18) defining $\mathcal{S}_{\boldsymbol{n}_1}^{1,\epsilon}$, we obtain the following respective expansions for the Günter tangential derivative, the operators $\Lambda_{1,\epsilon}$ and $\Lambda_{2,\epsilon,\boldsymbol{n}_1}$

$$\mathcal{M}_{\boldsymbol{n}_1} \boldsymbol{u}_\ell := \sum_m \begin{pmatrix} 0 & -\dfrac{im}{\mathrm{R}} \\ \dfrac{im}{\mathrm{R}} & 0 \end{pmatrix} \boldsymbol{u}_{\ell,m} e^{im\theta}, \tag{36}$$

$$\Lambda_{1,\epsilon} \boldsymbol{u}_\ell := i\rho\omega^2 \sum_m \begin{pmatrix} \xi_p^\epsilon & 0 \\ 0 & \xi_s^\epsilon \end{pmatrix} \boldsymbol{u}_{\ell,m} e^{im\theta}, \tag{37}$$

$$\Lambda_{2,\epsilon,\boldsymbol{n}_1}\boldsymbol{u}_\ell := -i\sum_m \begin{pmatrix} 0 & -\frac{im}{\mathrm{R}}\xi_p^\epsilon \\ \frac{im}{\mathrm{R}}\xi_s^\epsilon & 0 \end{pmatrix} \boldsymbol{u}_{\ell,m}e^{im\theta}, \tag{38}$$

when considering $\xi_{\{p,s\}}^\epsilon = \dfrac{1}{\kappa_{\{p,s\},\epsilon}}\left(1-(\dfrac{m}{\kappa_{\{p,s\},\epsilon}\mathrm{R}})^2\right)^{-1/2}$. Finally, from (15) we deduce

$$\mathcal{S}_{\boldsymbol{n}_1}^{1,\epsilon}\boldsymbol{u}_\ell := \sum_m \mathcal{S}_{\boldsymbol{n}_1,m}^{1,\epsilon}\boldsymbol{u}_\ell e^{im\theta}, \tag{39}$$

with $\delta = 1+\dfrac{m^2}{\mathrm{R}^2}\xi_p^\epsilon\xi_s^\epsilon$ and

$$\mathcal{S}_{\boldsymbol{n}_1,m}^{1,\epsilon} = \frac{i\rho\omega^2}{\delta}\begin{pmatrix} \xi_p^\epsilon & \frac{m}{\mathrm{R}}(\xi_p^\epsilon\xi_s^\epsilon - 2\frac{\delta}{\kappa_s^2}) \\ -\frac{m}{\mathrm{R}}(\xi_p^\epsilon\xi_s^\epsilon - 2\frac{\delta}{\kappa_s^2}) & \xi_s^\epsilon \end{pmatrix}. \tag{40}$$

Remark 1. *By definition of the traction operator* (4) *and of the high-order non-local transmission operator* (20)*, we deduce that on the surface* Γ *with normal* $\boldsymbol{n}_0 = -\boldsymbol{n}_1$ *we have for* $m \in \mathbb{N}$

$$\mathcal{T}_{\boldsymbol{n}_0,m} = -\mathcal{T}_{\boldsymbol{n}_1,m}, \tag{41}$$

and

$$\mathcal{S}_{\boldsymbol{n}_0,m}^{1,\epsilon} = \frac{i\rho\omega^2}{\delta}\begin{pmatrix} \xi_p^\epsilon & -\frac{m}{\mathrm{R}}(\xi_p^\epsilon\xi_s^\epsilon - 2\frac{\delta}{\kappa_s^2}) \\ \frac{m}{\mathrm{R}}(\xi_p^\epsilon\xi_s^\epsilon - 2\frac{\delta}{\kappa_s^2}) & \xi_s^\epsilon \end{pmatrix}. \tag{42}$$

3.3. Determination of the iteration matrix

We develop the iteration matrix $\mathcal{A}$ thanks to the Fourier expansion

$$\mathcal{A}\boldsymbol{u}_\ell = \sum_m \mathcal{A}_m\boldsymbol{u}_\ell e^{im\theta}. \tag{43}$$

Using equations (21)–(22) satisfied by $\boldsymbol{g}_0^{(p)}$ and $\boldsymbol{g}_1^{(p)}$, we first determine $\mathcal{A}_0$ and $\mathcal{A}_1$ mode-by-mode. Let us begin by expanding $\boldsymbol{g}_0^{(p)}$ and $\boldsymbol{g}_1^{(p)}$

$$\boldsymbol{g}_0^{(p)} := \sum_m \boldsymbol{g}_{0,m}^{(p)}e^{im\theta}, \quad \boldsymbol{g}_1^{(p)} := \sum_m \boldsymbol{g}_{1,m}^{(p)}e^{im\theta}. \tag{44}$$

In addition, using (21) and Remark 1, the surface field $\boldsymbol{g}_0^{(p)}$ satisfies

$$\begin{cases} \boldsymbol{g}_0^{(p)} &= -(\mathcal{T}_{\boldsymbol{n}_1}+\mathcal{S}_{\boldsymbol{n}_0}^{1,\epsilon})\boldsymbol{u}_0^{(p+1)}, \\ \boldsymbol{g}_0^{(p)} &= -(\mathcal{T}_{\boldsymbol{n}_1}+\mathcal{S}_{\boldsymbol{n}_0}^{1,\epsilon})\boldsymbol{u}_1^{(p)}. \end{cases} \tag{45}$$

We deduce from expansions of $\boldsymbol{u}_\ell$ (30), $\boldsymbol{g}_\ell$ (44) and the definitions of p_ℓ and q_ℓ (31), for $\ell = 0, 1$, the following relations

$$\boldsymbol{g}_0^{(p)} = \sum_m e^{im\theta}\begin{pmatrix} A_{0,m} & A_{1,m} \\ A_{2,m} & A_{3,m} \end{pmatrix}\begin{pmatrix} \alpha_{p,m}^{(p+1)} \\ \alpha_{s,m}^{(p+1)} \end{pmatrix}, \tag{46}$$

and

$$\boldsymbol{g}_0^{(p)} = \sum_m e^{im\theta}\begin{pmatrix} B_{0,m} & B_{1,m} \\ B_{2,m} & B_{3,m} \end{pmatrix}\begin{pmatrix} \beta_{p,m}^{(p)} \\ \beta_{s,m}^{(p)} \end{pmatrix}, \tag{47}$$

with

$$\begin{cases} A_{0,m} = \mathbf{a}_{p,m}\cdot\mathbf{h}_p, \ A_{1,m} = \mathbf{b}_{s,m}\cdot\mathbf{h}_s, \ A_{2,m} = \mathbf{b}_{p,m}\cdot\mathbf{h}_p, \ A_{3,m} = -\mathbf{a}_{s,m}\cdot\mathbf{h}_s, \\ B_{0,m} = \mathbf{a}_{p,m}\cdot\mathbf{j}_p, \ B_{1,m} = \mathbf{b}_{s,m}\cdot\mathbf{j}_s, \ B_{2,m} = \mathbf{b}_{p,m}\cdot\mathbf{j}_p, \ B_{3,m} = -\mathbf{a}_{s,m}\cdot\mathbf{j}_s, \end{cases} \tag{48}$$

where the following notations were introduced:

$$\begin{cases} \mathbf{a}_{p,m} = \left(\dfrac{\rho\omega^2}{\delta}, \kappa_p(\dfrac{2\mu}{r} - \dfrac{i\rho\omega^2}{\delta}\xi_p^\epsilon)\right), & \mathbf{b}_{p,m} = \dfrac{im}{r}\left(\dfrac{2\mu}{r} - \dfrac{i\rho\omega^2}{\delta}\xi_s^\epsilon, -\dfrac{\rho\omega^2}{\delta}\xi_p^\epsilon\xi_s^\epsilon\kappa_p\right), \\ \mathbf{a}_{s,m} = \left(\dfrac{\rho\omega^2}{\delta}, \kappa_s(\dfrac{2\mu}{r} - \dfrac{i\rho\omega^2}{\delta}\xi_s^\epsilon)\right), & \mathbf{b}_{s,m} = \dfrac{im}{r}\left(\dfrac{2\mu}{r} - \dfrac{i\rho\omega^2}{\delta}\xi_p^\epsilon, -\dfrac{\rho\omega^2}{\delta}\xi_p^\epsilon\xi_s^\epsilon\kappa_s\right), \\ \mathbf{h}_p = \left(H_m^1(\kappa_p r), H_m^{1'}(\kappa_p r)\right), & \mathbf{h}_s = \left(H_m^1(\kappa_s r), H_m^{1'}(\kappa_s r)\right), \\ \mathbf{j}_p = \left(J_m(\kappa_p r), J_m'(\kappa_p r)\right), & \mathbf{j}_s = \left(J_m(\kappa_s r), J_m'(\kappa_s r)\right). \end{cases} \tag{49}$$

Similarly, noting that

$$\begin{cases} \boldsymbol{g}_1^{(p)} = (\mathcal{T}_{\boldsymbol{n}_1} - \mathcal{S}_{\boldsymbol{n}_1}^{1,\epsilon})\boldsymbol{u}_1^{(p+1)}, \\ \boldsymbol{g}_1^{(p)} = (\mathcal{T}_{\boldsymbol{n}_1} - \mathcal{S}_{\boldsymbol{n}_1}^{1,\epsilon})\boldsymbol{u}_0^{(p)}, \end{cases} \tag{50}$$

we obtain the expansions of $\boldsymbol{g}_1^{(p)}$

$$\boldsymbol{g}_1^{(p)} = \sum_m e^{im\theta}\begin{pmatrix} B_{4,m} & B_{5,m} \\ B_{6,m} & B_{7,m} \end{pmatrix}\begin{pmatrix} \beta_{p,m}^{(p+1)} \\ \beta_{s,m}^{(p+1)} \end{pmatrix}, \tag{51}$$

and

$$\boldsymbol{g}_1^{(p)} = \sum_m e^{im\theta}\begin{pmatrix} A_{4,m} & A_{5,m} \\ A_{6,m} & A_{7,m} \end{pmatrix}\begin{pmatrix} \alpha_{p,m}^{(p)} \\ \alpha_{s,m}^{(p)} \end{pmatrix}, \tag{52}$$

with

$$\begin{cases} B_{4,m} = -\mathbf{c}_{p,m}\cdot\mathbf{j}_p, \quad B_{5,m} = \mathbf{d}_{s,m}\cdot\mathbf{j}_s, \quad B_{6,m} = \mathbf{d}_{p,m}\cdot\mathbf{j}_p, \quad B_{7,m} = \mathbf{c}_{s,m}\cdot\mathbf{j}_s, \\ A_{4,m} = -\mathbf{c}_{p,m}\cdot\mathbf{h}_p, \quad A_{5,m} = \mathbf{d}_{s,m}\cdot\mathbf{h}_s, \quad A_{6,m} = \mathbf{d}_{p,m}\cdot\mathbf{h}_p, \quad A_{7,m} = \mathbf{c}_{s,m}\cdot\mathbf{h}_s, \end{cases} \tag{53}$$

when considering

$$\begin{cases} \mathbf{c}_{p,m} = \left(\dfrac{\rho\omega^2}{\delta}, \kappa_p(\dfrac{2\mu}{r} + \dfrac{i\rho\omega^2}{\delta}\xi_p^\epsilon)\right), & \mathbf{d}_{p,m} = \dfrac{im}{r}\left(-\dfrac{2\mu}{r} - \dfrac{i\rho\omega^2}{\delta}\xi_s^\epsilon, \dfrac{\rho\omega^2}{\delta}\xi_p^\epsilon\xi_s^\epsilon\kappa_p\right), \\ \mathbf{c}_{s,m} = \left(\dfrac{\rho\omega^2}{\delta}, \kappa_s(\dfrac{2\mu}{r} + \dfrac{i\rho\omega^2}{\delta}\xi_s^\epsilon)\right), & \mathbf{d}_{s,m} = \dfrac{im}{r}\left(-\dfrac{2\mu}{r} - \dfrac{i\rho\omega^2}{\delta}\xi_p^\epsilon, \dfrac{\rho\omega^2}{\delta}\xi_p^\epsilon\xi_s^\epsilon\kappa_s\right). \end{cases} \tag{54}$$

Now, we identify the two relations (46)–(47) for $\boldsymbol{g}_0^{(p)}$, respectively (51)–(52) for $\boldsymbol{g}_1^{(p)}$, to obtain

$$\begin{pmatrix} \alpha_m^{p,n+1} \\ \alpha_m^{s,n+1} \end{pmatrix} = \begin{pmatrix} A_{0,m} & A_{1,m} \\ A_{2,m} & A_{3,m} \end{pmatrix}^{-1}\begin{pmatrix} B_{0,m} & B_{1,m} \\ B_{2,m} & B_{3,m} \end{pmatrix}\begin{pmatrix} \beta_m^{p,n} \\ \beta_m^{s,n} \end{pmatrix}, \tag{55}$$

$$\begin{pmatrix} \beta_m^{p,n+1} \\ \beta_m^{s,n+1} \end{pmatrix} = \begin{pmatrix} B_{4,m} & B_{5,m} \\ B_{6,m} & B_{7,m} \end{pmatrix}^{-1}\begin{pmatrix} A_{4,m} & A_{5,m} \\ A_{6,m} & A_{7,m} \end{pmatrix}\begin{pmatrix} \alpha_m^{p,n} \\ \alpha_m^{s,n} \end{pmatrix}. \tag{56}$$

From definitions (47)–(56)–(52), we deduce

$$\boldsymbol{g}_{0,m}^{(p+1)} = \begin{pmatrix} B_{0,m} & B_{1,m} \\ B_{2,m} & B_{3,m} \end{pmatrix}\begin{pmatrix} B_{4,m} & B_{5,m} \\ B_{6,m} & B_{7,m} \end{pmatrix}^{-1}\boldsymbol{g}_{1,m}^{(p)} := \mathcal{A}_{1,m}\boldsymbol{g}_{1,m}^{(p)}, \tag{57}$$

and with (52)–(55)–(47), we get

$$\boldsymbol{g}_{1,m}^{(p+1)} = \begin{pmatrix} A_{4,m} & A_{5,m} \\ A_{6,m} & A_{7,m} \end{pmatrix}\begin{pmatrix} A_{0,m} & A_{1,m} \\ A_{2,m} & A_{3,m} \end{pmatrix}^{-1}\boldsymbol{g}_{0,m}^{(p)} := \mathcal{A}_{0,m}\boldsymbol{g}_{0,m}^{(p)}. \tag{58}$$

Finally, we have the following iterative scheme

$$\boldsymbol{g}_m^{(p+1)} := \begin{pmatrix} \boldsymbol{g}_{1,m}^{(p+1)} \\ \boldsymbol{g}_{0,m}^{(p+1)} \end{pmatrix} = \mathcal{A}_m\boldsymbol{g}_m^{(p)} := \begin{pmatrix} \mathbf{0}_2 & \mathcal{A}_{0,m} \\ \mathcal{A}_{1,m} & \mathbf{0}_2 \end{pmatrix}\begin{pmatrix} \boldsymbol{g}_{1,m}^{(p)} \\ \boldsymbol{g}_{0,m}^{(p)} \end{pmatrix}. \tag{59}$$

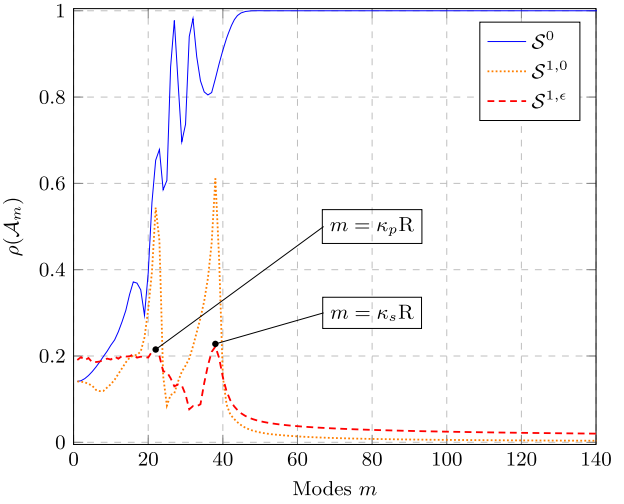


Fig. 2. Spectral radius of the modal iteration matrix $\mathcal{A}_m$ with respect to the mode m. $f = 6\,\mathrm{Hz}$, $\mathrm{R} = 1\,\mathrm{m}$, $\lceil \kappa_p \rceil = 22\,\mathrm{m}^{-1}$, $\lceil \kappa_s \rceil = 38\,\mathrm{m}^{-1}$.

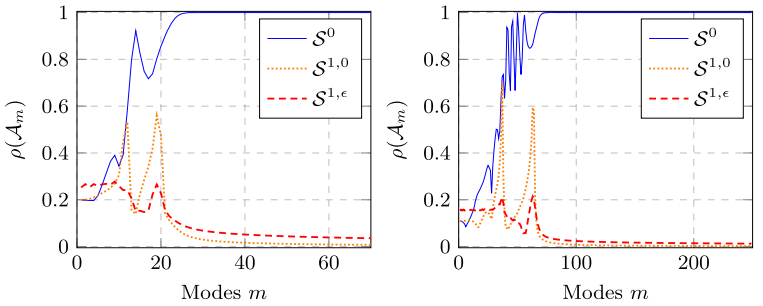


Fig. 3. Spectral radius of the modal iteration matrix $\mathcal{A}_m$ with respect to the mode m for $\mathrm{R} = 1\,\mathrm{m}$ at two frequencies $f = 3\,\mathrm{Hz}$ (left) and $f = 10\,\mathrm{Hz}$ (right), corresponding to $\lceil \kappa_p \rceil = 11\,\mathrm{m}^{-1}$, $\lceil \kappa_s \rceil = 19\,\mathrm{m}^{-1}$ (left) and $\lceil \kappa_p \rceil = 37\,\mathrm{m}^{-1}$, $\lceil \kappa_s \rceil = 63\,\mathrm{m}^{-1}$ (right).

3.4. Spectrum of the iteration matrix

The convergence properties of the DDM are strongly related to the spectrum of the iteration operator $(I - \mathcal{A})$. First, let us numerically study the spectrum of the modal matrices $\mathcal{A}_m$ in the case where Ω_1 is the unit disk. The mechanical parameters are normalized and defined such that the wavenumbers satisfy $\kappa_s = \sqrt{3}\kappa_p$ (i.e. $\lambda = 1\,\mathrm{Pa}$, $\mu = 1\,\mathrm{Pa}$, $\rho = 1\,\mathrm{Kg/m^3}$). We fix the maximal number of modes $m^{\max} = 4\lfloor \kappa_s \rfloor$, where $\lfloor x \rfloor$ denotes the floor function of a real x.

We report in Figs. 2–4 the modal spectral radius $\rho(\mathcal{A}_m)$ with respect to the modes m corresponding to the transmission operators $\mathcal{S}^0$, $\mathcal{S}^{1,0}$ and $\mathcal{S}^{1,\epsilon}$ (where $\mathcal{S}^{1,0}$ is the non-local HO-TBC operator taking $\epsilon_p = \epsilon_s = 0$) for different frequencies. We observe that the behavior of the different spectral radius is independent of the frequency in the three zones (propagative, transition and evanescent) of modes. The LO-TBC operator $\mathcal{S}^0$ acts on propagating modes only ($m \ll \kappa_p \mathrm{R}$). Moreover, as the Després condition in the Helmholtz case [6], the spectral radius of $\mathcal{A}_m$ associated with $\mathcal{S}^0$ is equal to 1 for evanescent modes ($m \gg \kappa_s \mathrm{R}$). Applying the new non-local HO-TBC without damping related to $\mathcal{S}^{1,0}$, the convergence rate is optimal (i.e. the spectral radius tends to 0) for the evanescent modes and an improvement over the LO-TBC in the hyperbolic part ($m \ll \kappa_p \mathrm{R}$) is observed. Furthermore, the singularities of the square-root operators (see (16) and (17)) in the transition zone of creeping modes ($m \approx \kappa_p \mathrm{R}$ and $m \approx \kappa_s \mathrm{R}$) lead to two expected amplitude peaks. Finally, adding the damping parameters $\epsilon_{\{p,s\}}$, the non-local HO-TBC leads to a smaller spectral radius for the grazing modes than without damping. A slight increase of the spectral radius for evanescent modes appears but it is not damaging as we will see in the next section. The same behavior is observed at other frequencies and other wavenumber ratios: see Figs. 3, 4.

Regarding Figs. 2–4, we may wonder about the value of the limit of the spectral radius $\rho(A_m)$ associated with the non-local HO-TBC for large modes m. Theorem 1 answers this question.

Theorem 1. *When $m \to +\infty$, the spectrum of the iteration matrix $\mathcal{A}_m$ associated with the non-local HO-TBC goes to* 0.

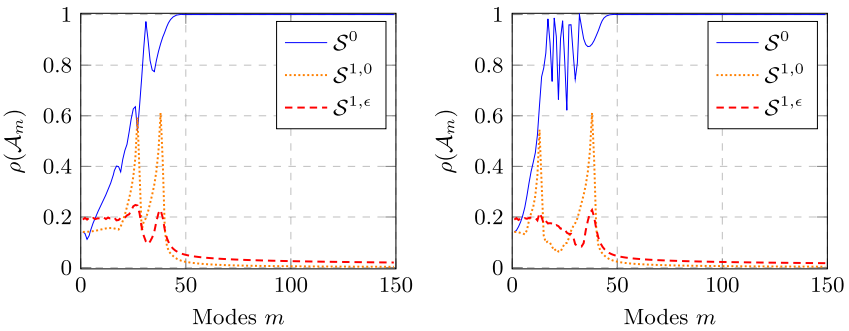


Fig. 4. Spectral radius of the modal iteration matrix $\mathcal{A}_m$ with respect to the mode m for $\mathrm{R} = 1\,\mathrm{m}$, $f = 6\,\mathrm{Hz}$, $\lceil \kappa_s \rceil = 38\,\mathrm{m}^{-1}$, $\kappa_s \simeq \sqrt{2}\kappa_p$ (left) and $\kappa_s = 3\kappa_p$ (right), corresponding to $\lceil \kappa_p \rceil = 27\,\mathrm{m}^{-1}$ (left) and $\lceil \kappa_p \rceil = 13\,\mathrm{m}^{-1}$ (right).

Proof 1. The proof will be held in three parts. First, we compute the coefficients of the iteration matrix $\mathcal{A}_m$ and give an approximation of them for large modes. Then, we express the eigenvalues of $\mathcal{A}_m$. Finally, we detail the limit of the eigenvalues associated with evanescent modes.

1. Make the iteration matrix explicit.

The iteration matrix is given by

$$\mathcal{A}_m = \begin{pmatrix} 0 & 0 & a_m & b_m \\ 0 & 0 & c_m & d_m \\ e_m & f_m & 0 & 0 \\ g_m & h_m & 0 & 0 \end{pmatrix}, \tag{60}$$

where the coefficients $a_m, b_m, c_m, d_m, e_m, f_m, g_m, h_m$ are detailed in Appendix A.

Let us focus on approximations of Bessel and Hankel functions when m goes to infinity. We recall the following approximations for the first and second kind Bessel functions when $m \to +\infty$ [1]

$$J_m(\kappa r) \sim \frac{1}{\sqrt{2\pi m}} \left(\frac{e\kappa r}{2m}\right)^m, \tag{61}$$

$$Y_m(\kappa r) \sim -\sqrt{\frac{2}{\pi m}} \left(\frac{2m}{e\kappa r}\right)^m. \tag{62}$$

The relation $m! \sim \sqrt{2\pi m}\left(\frac{m}{e}\right)^m$ allows to get equivalently

$$J_m(\kappa r) \sim \frac{1}{m!} \left(\frac{\kappa r}{2}\right)^m, \quad Y_m(\kappa r) \sim -\frac{(m-1)!}{\pi} \left(\frac{2}{\kappa r}\right)^m. \tag{63}$$

Thus, in the following, recalling that $H_m(\kappa r) = J_m(\kappa r) + iY_m(\kappa r)$, we will use

$$H_m(\kappa r) \sim -i\sqrt{\frac{2}{\pi m}} \left(\frac{2m}{e\kappa r}\right)^m, \tag{64}$$

$$J'_m(\kappa r) \sim \sqrt{\frac{m}{2\pi}} \left(\frac{e\kappa r}{2m}\right)^m \frac{1}{\kappa r}, \tag{65}$$

and

$$H'_m(\kappa r) \sim i\sqrt{\frac{2m}{\pi}} \left(\frac{2m}{e\kappa r}\right)^m \frac{1}{\kappa r}. \tag{66}$$

Let us denote $d_0 = c_0/m$, $d_1 = c_1/(\kappa_p \mathrm{R})$, $d_2 = c_2/(\kappa_s \mathrm{R})$ and $d_3 = c_3 m/(\kappa_p \kappa_s \mathrm{R}^2)$ with c_0, c_1, c_2, c_3 defined in (A.11). We detail how to obtain an estimation of a_m for large modes m. The other coefficients are approximated similarly. For the sake of simplicity, we denote in the following $H_{\{p,s\}} = H_m(\kappa_{\{p,s\}} r)$ and $H'_{\{p,s\}} = H'_m(\kappa_{\{p,s\}} r)$. By definition (A.5)–(A.9), the numerator of a_m is given by

$$\mathrm{Num}_{a_m} = c_0 H_p H_s + c_1 H'_p H_s + c_2 H_p H'_s + c_3 H'_p H'_p. \tag{67}$$

Taking Hankel function approximations (64)–(66) we obtain

$$\mathrm{Num}_{a_m} \sim \frac{2}{\pi}\left(\frac{2m}{e\sqrt{\kappa_p\kappa_s}\mathrm{R}}\right)^{2m}[-d_0+d_1+d_2-d_3]. \tag{68}$$

Similarly, by definition (A.5)–(A.7), the denominator of a_m

$$\mathrm{Den}_{a_m} = c_0 H_p H_s + c_1 H_p' H_s + c_2 H_p H_s' + c_3 H_p' H_s', \tag{69}$$

is approximated thanks to (64)–(66) by

$$\mathrm{Den}_{a_m} \sim \frac{2}{\pi}\left(\frac{2m}{e\sqrt{\kappa_p\kappa_s}R}\right)^{2m}\left[-\frac{b_0}{m}+\frac{b_1}{\kappa_p\mathrm{R}}+\frac{b_2}{\kappa_s\mathrm{R}}-\frac{b_3 m}{\kappa_p\kappa_s\mathrm{R}^2}\right]. \tag{70}$$

We finally obtain the following approximation for large modes m

$$a_m \sim \left[\frac{-d_0+d_1+d_2-d_3}{-b_0/m+b_1/(\kappa_p\mathrm{R})+b_2/(\kappa_s\mathrm{R})-b_3 m/(\kappa_p\kappa_s\mathrm{R}^2)}\right]. \tag{71}$$

The other approximations are obtained in the same way and are given by

$$\begin{aligned}
b_m &\sim \frac{-2\rho^2\omega^4\xi_p^\epsilon}{\delta\mathrm{R}}\left[\frac{1}{-b_0/m+b_1/(\kappa_p\mathrm{R})+b_2/(\kappa_s\mathrm{R})-b_3 m/(\kappa_p\kappa_s\mathrm{R}^2)}\right],\\
c_m &\sim \frac{2\rho^2\omega^4\xi_s^\epsilon}{\delta\mathrm{R}}\left[\frac{1}{-b_0/m+b_1/(\kappa_p\mathrm{R})+b_2/(\kappa_s\mathrm{R})-b_3 m/(\kappa_p\kappa_s\mathrm{R}^2)}\right],\\
d_m &\sim \left[\frac{d_4+d_5+d_6+d_7}{-b_0/m+b_1/(\kappa_p\mathrm{R})+b_2/(\kappa_s\mathrm{R})-b_3 m/(\kappa_p\kappa_s\mathrm{R}^2)}\right],\\
e_m &\sim \left[\frac{d_4+d_5+d_6+d_7}{b_4/m+b_5/(\kappa_p\mathrm{R})+b_6/(\kappa_s\mathrm{R})+b_3 m/(\kappa_p\kappa_s\mathrm{R}^2)}\right],\\
f_m &\sim \frac{-2\rho^2\omega^4\xi_p^\epsilon}{\delta\mathrm{R}}\left[\frac{1}{b_4/m+b_5/(\kappa_p\mathrm{R})+b_6/(\kappa_s\mathrm{R})+b_3 m/(\kappa_p\kappa_s\mathrm{R}^2)}\right],\\
g_m &\sim \frac{2\rho^2\omega^4\xi_s^\epsilon}{\delta\mathrm{R}}\left[\frac{1}{b_4/m+b_5/(\kappa_p\mathrm{R})+b_6/(\kappa_s\mathrm{R})+b_3 m/(\kappa_p\kappa_s\mathrm{R}^2)}\right],\\
h_m &\sim \left[\frac{d_0+d_1+d_2+d_3}{b_4/m+b_5/(\kappa_p\mathrm{R})+b_6/(\kappa_s\mathrm{R})+b_3 m/(\kappa_p\kappa_s\mathrm{R}^2)}\right],
\end{aligned} \tag{72}$$

with $d_4 = c_4/m$, $d_5 = c_5/(\kappa_p R)$, $d_6 = c_6/(\kappa_s\mathrm{R})$ and $d_7 = c_7 m/(\kappa_p\kappa_s\mathrm{R}^2)$ when considering c_0, c_1, c_2, c_3 defined in (A.11).

When $m \to \infty$, we have $\xi_p^\epsilon \sim \xi_s^\epsilon \sim \frac{-i\mathrm{R}}{m}$. We deduce $c_m \sim -b_m$, $g_m \sim -f_m$ and

$$\mathcal{A}_m \sim \begin{pmatrix} 0 & 0 & a_m & b_m \\ 0 & 0 & -b_m & d_m \\ e_m & f_m & 0 & 0 \\ -f_m & h_m & 0 & 0 \end{pmatrix}. \tag{73}$$

2. Make the eigenvalues explicit.

The eigenvalues of $\mathcal{A}_m$ (73) are $\{\pm\lambda_{1,m}, \pm\lambda_{2,m}\}$ with

$$\begin{aligned}
\lambda_{1,m} &= \frac{1}{\sqrt{2}}\sqrt{a_m e_m - 2b_m f_m + d_m h_m + \Delta_m},\\
\lambda_{2,m} &= \frac{1}{\sqrt{2}}\sqrt{a_m e_m - 2b_m f_m + d_m h_m - \Delta_m},
\end{aligned} \tag{74}$$

and $\Delta_m := \sqrt{(a_m e_m - d_m h_m)^2 - 4(a_m f_m + b_m h_m)(b_m e_m + d_m f_m)}$. For the sake of simplicity, we omit the index m in the following. Denoting

$$\mathrm{invDen} = \left[(-\frac{b_0}{m}+\frac{b_1}{\kappa_p\mathrm{R}}+\frac{b_2}{\kappa_s\mathrm{R}}-\frac{b_3 m}{\kappa_p\kappa_s\mathrm{R}^2})(\frac{b_4}{m}+\frac{b_5}{\kappa_p\mathrm{R}}+\frac{b_6}{\kappa_s\mathrm{R}}+\frac{b_3 m}{\kappa_p\kappa_s\mathrm{R}^2})\right]^{-1}, \tag{75}$$

we obtain

$$ae - 2bf + dh \sim \text{invDen}\left(-2(d_0+d_3)(d_4+d_7)+2(d_1+d_2)(d_5+d_6) - 8\frac{\rho^4\omega^8\xi^2}{\delta^2 \mathrm{R}^2}\right), \tag{76}$$

$$(ae - dh)^2 \sim \text{invDen}^2\left[-2(d_0+d_3)(d_5+d_6)+2(d_1+d_2)(d_4+d_7)\right]^2, \tag{77}$$

and

$$(af + bh)(be + df) \sim \text{invDen}^2 \frac{16\rho^4\omega^8\xi^2}{\delta^2\mathrm{R}^2}(d_1+d_2)(d_5+d_6).$$

Finally, substituting d_j, $j = 0, \ldots, 7$, by their estimations, we get

$$\text{invDen} \sim \frac{m^2\delta^2 r^4/(\rho^4\omega^8)}{-(\mathrm{R}^2 - m^2\xi_p^\epsilon\xi_s^\epsilon)^2 - 2imr(\mathrm{R}^2 - m^2\xi_p^\epsilon\xi_s^\epsilon)(\xi_p^\epsilon + \xi_s^\epsilon) + \mathrm{R}^2 m^2(\xi_p^\epsilon + \xi_s^\epsilon)^2 + 16\frac{m^2\delta^2\mathrm{R}^2}{\kappa_s^4}}, \tag{78}$$

$$ae - 2bf + dh \sim 2\text{invDen}\rho^2\omega^4\left(\frac{16\mu^2}{r^4} - \frac{\rho^2\omega^4}{m^2\delta^2}(1 - \frac{m^2}{\mathrm{R}^2}\xi_p\xi_s)^2 + \frac{\rho^2\omega^4(\xi_s^\epsilon - \xi_p^\epsilon)^2}{(\delta r)^2} - \frac{4\rho^2\omega^4\xi^2}{(\delta r)^2}\right), \tag{79}$$

and

$$\Delta^2 \sim -\frac{16\rho^6\omega^{12}\text{invDen}^2}{(r\delta)^2}\left(\frac{64\mu^2\xi^2}{r^4} + (\xi_s^\epsilon - \xi_p^\epsilon)^2\left(\frac{(1-\frac{m^2}{r^2}\xi_p\xi_s)^2}{m^2\delta^2} + \frac{4\rho\omega^2\xi^2}{\delta^2 r^2}\right)\right). \tag{80}$$

3. Asymptotic behavior of the eigenvalues.
Let us first remark that $\xi_{\{p,s\}}^\epsilon$ can be written for large m as

$$\xi_{\{p,s\}}^\epsilon = \frac{-i\mathrm{R}}{m}\left(1 - \left(\frac{\kappa_{\{p,s\},\epsilon}\mathrm{R}}{m}\right)^2\right)^{-1/2}. \tag{81}$$

A Taylor expansion of the square-root leads to

$$\xi_{\{p,s\}}^\epsilon = -\frac{i\mathrm{R}}{m} - \frac{i\kappa_{\{p,s\},\epsilon}^2}{2}\frac{\mathrm{R}^3}{m^3} \sim -\frac{i\mathrm{R}}{m} = O(m^{-1}), \tag{82}$$

and we deduce

$$\delta = 1 + \frac{m^2}{\mathrm{R}^2}\xi_p^\epsilon\xi_s^\epsilon \sim -\frac{R^2}{2m^2}(\kappa_{p,\epsilon}^2 + \kappa_{s,\epsilon}^2) = O(m^{-2}). \tag{83}$$

We detail also the following expressions which are useful for computations

$$(\xi_p^\epsilon + \xi_s^\epsilon) \sim -\frac{2iR}{m} = O(m^{-1}), \tag{84}$$

$$(\xi_s^\epsilon - \xi_p^\epsilon) \sim \frac{iR^3}{2m^3}(\kappa_{p,\epsilon}^2 - \kappa_{s,\epsilon}^2) = O(m^{-3}). \tag{85}$$

We will now approximate invDen, $ad - 2be + cf$ and Δ using (82)–(83)–(84)–(85)

$$\begin{aligned} \text{invDen} &\sim -\frac{m^2\delta^2}{16\rho^4\omega^8}, \\ ae - 2bf + dh &\sim -2\frac{m^2\delta^2}{(\kappa_s\mathrm{R})^4} \sim -\frac{1}{2m^2\kappa_s^4}\left(\kappa_{p,\epsilon}^2 + \kappa_{s,\epsilon}^2\right)^2, \\ \Delta &\sim \pm\frac{2m\delta}{(\kappa_s\mathrm{R})^2} \sim \pm\frac{1}{m\kappa_s^2}(\kappa_{p,\epsilon}^2 + \kappa_{s,\epsilon}^2). \end{aligned} \tag{86}$$

We deduce that $\lambda_{\{1,2\},m} = O(m^{-1/2})$ with the definition of the eigenvalues (74). This ends the proof.

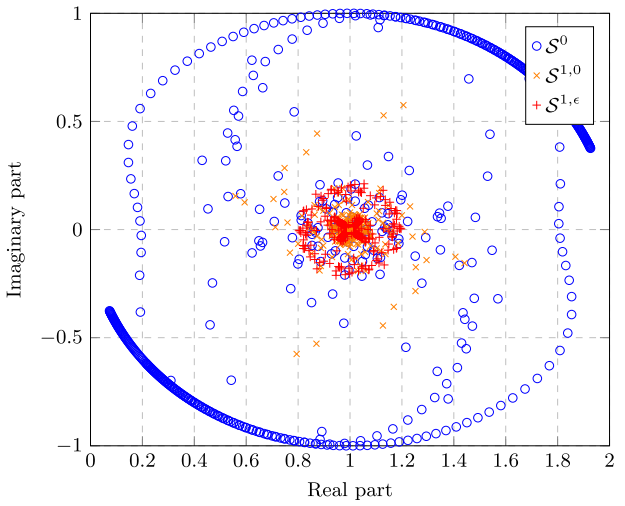


Fig. 5. Eigenvalues of $(\mathcal{I}-\mathcal{A})$ in the complex plane for the different transmission operators. $f=6\,\mathrm{Hz}$, $\mathrm{R}=1\,\mathrm{m}$, $\lceil\kappa_p\rceil=22\,\mathrm{m}^{-1}$, $\lceil\kappa_s\rceil=38\,\mathrm{m}^{-1}$, $m^{\max}=4\lfloor\kappa_s\rfloor$.

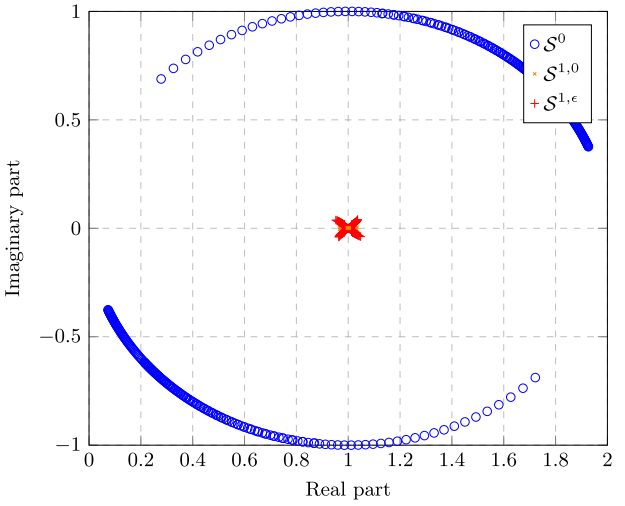


Fig. 6. Eigenvalues of $(\mathcal{I}-\mathcal{A})$ in the complex plane for evanescent modes. $f=6\,\mathrm{Hz}$, $\mathrm{R}=1\,\mathrm{m}$, $\lceil\kappa_p\rceil=22\,\mathrm{m}^{-1}$, $\lceil\kappa_s\rceil=38\,\mathrm{m}^{-1}$, $45\le m\le m^{\max}$.

3.5. Krylov subspace solvers

We use the GMRES iterative algorithm to solve (10). It is well known that the GMRES solver converges faster when an eigenvalue clustering around an accumulation point (in the complex plane) occurs. The eigenvalues of the operator $(\mathcal{I}-\mathcal{A})$ are given by $\mu^{\pm}_{\ell,m}=1\pm\lambda_{\ell,m}$, for $\ell=0,1$ and all modes $m\in\mathbb{N}$. We report in Fig. 5 the eigenvalue distribution for the different transmission operators $\mathcal{S}^0$, $\mathcal{S}^{1,0}$ and $\mathcal{S}^{1,\epsilon}$. We take the same physical parameters as previously and fix $f=6\,\mathrm{Hz}$.

We zoom in Fig. 6 on the modes $45\le m\le m^{\max}$ in order to better analyze the spectrum in the elliptic part. The eigenvalues associated with the LO-TBC $\mathcal{S}^0$ spread out in the complex plane. When comparing Figs. 5 and 6, we deduce that the eigenvalues associated with evanescent modes are distributed on arcs of circle of radius 1 whereas the one associated to propagative and grazing modes are located inside the unit disk. There are two accumulation points: $(0,0)$ and $(2,0)$. For the HO-TBC ($\mathcal{S}^{1,\epsilon}$), we observe an excellent eigenvalue clustering around the point $(1,0)$ for all modes, and in particular for large modes as expected from Theorem 1. We also see the great influence of the damping parameters. Without damping (considering $\mathcal{S}^{1,0}$), we note a spreading of some eigenvalues associated with the grazing modes (in agreement with the results of Fig. 2). Let us now explain the localization procedure of the HO transmission operator.

4. Localization of the high-order transmission operator by complex Padé approximants

The HO transmission operator (20) is non-local. More particularly, the inverse of the square-root operator implied in $\Lambda_{1,\epsilon}$ (16) and $\Lambda_{2,\epsilon,\boldsymbol{n}}$ (17) is non-local. In a finite element context, it involves implementing full matrices at the transmission boundaries. To get a local and uniform representation of the function $(1+z)^{-1/2}$ (20), we use complex rational Padé approximants with a rotating branch-cut technique of angle α [9]: for $z \in \mathbb{C}$, one has

$$(1+z)^{-1/2} \approx \sum_{\ell=0}^{L-1} \frac{R_\ell^\alpha}{S_\ell^\alpha + z}, \tag{87}$$

where

$$\begin{cases} R_\ell^\alpha \;=\; e^{i\alpha/2} c_\ell, \quad S_\ell^\alpha \;=\; 1 + e^{i\alpha}(-1+d_\ell), \quad \ell = 0,\dots,L-1, \\ c_\ell \;=\; \dfrac{d_\ell}{L}, \qquad\quad d_\ell \;=\; 1+\tan^2\Big(\dfrac{\pi}{2L}(\dfrac{1}{2}+\ell)\Big), \quad \ell = 0,\dots,L-1. \end{cases} \tag{88}$$

Finally, we propose the following regularized Padé-localized transmission boundary operator

$$\mathcal{S}_{\boldsymbol{n}}^{\widetilde{1,\epsilon}} = (I + \Lambda_{\widetilde{2,\epsilon},\boldsymbol{n}})^{-1} \Lambda_{\widetilde{1,\epsilon}} + 2\mu \mathcal{M}_{\boldsymbol{n}}, \tag{89}$$

with $\mathcal{M}_{\boldsymbol{n}}$ the Günter tangential derivative and

$$\Lambda_{\widetilde{1,\epsilon}} = i\rho\omega^2 \Bigg[\frac{1}{\kappa_{p,\epsilon}} \boldsymbol{n} \sum_{\ell=0}^{L-1} R_\ell^\alpha \left(\frac{\Delta_\Gamma}{\kappa_{p,\epsilon}^2} + S_\ell^\alpha \mathrm{I} \right)^{-1} (\boldsymbol{n} \cdot \mathrm{I}_{\boldsymbol{n}}) + \frac{1}{\kappa_{s,\epsilon}} \boldsymbol{\tau} \sum_{\ell=0}^{L-1} R_\ell^\alpha \left(\frac{\Delta_\Gamma}{\kappa_{s,\epsilon}^2} + S_\ell^\alpha \mathrm{I} \right)^{-1} (\boldsymbol{\tau} \cdot \mathrm{I}_{\boldsymbol{\tau}}) \Bigg], \tag{90}$$

$$\begin{aligned} \Lambda_{\widetilde{2,\epsilon},\boldsymbol{n}} \;=\; -i \Bigg[& \left(\frac{1}{\kappa_{s,\epsilon}} \partial_s \sum_{\ell=0}^{L-1} R_\ell^\alpha \left(\frac{\Delta_\Gamma}{\kappa_{s,\epsilon}^2} + S_\ell^\alpha \mathrm{I} \right)^{-1} (\boldsymbol{n} \cdot \mathrm{I}_{\boldsymbol{n}}) \right) \boldsymbol{\tau} \\ & - \left(\frac{1}{\kappa_{p,\epsilon}} \partial_s \sum_{\ell=0}^{L-1} R_\ell^\alpha \left(\frac{\Delta_\Gamma}{\kappa_{p,\epsilon}^2} + S_\ell^\alpha \mathrm{I} \right)^{-1} (\boldsymbol{\tau} \cdot \mathrm{I}_{\boldsymbol{\tau}}) \right) \boldsymbol{n} \Bigg]. \end{aligned} \tag{91}$$

The low-order operator (13) is an approximation of order 0 of the high-order non-local operator (20) without damping noting that $\kappa_p^2 = \rho\omega^2(\lambda+2\mu)^{-1}$ and $\kappa_s^2 = \rho\omega^2\mu^{-1}$. By approximation of order 0, we mean replacing the surface differential operators by their first eigenvalue equals to zero. Moreover, noting that $\forall \alpha \in [0, 2\pi[$

$$\sum_{\ell=0}^{L-1} \frac{R_\ell^\alpha}{S_\ell^\alpha} \underset{L\to+\infty}{\longrightarrow} 1, \tag{92}$$

the 0th-order approximation of the regularized Padé-localized operator (89) tends to the low-order operator for large Padé-orders L. Let us analyze the effect of the Padé approximation on the spectrum of the matrices $(\mathcal{I} - \mathcal{A})$ and $\mathcal{A}$ for the model problem of Section 3. For a mode m, the transmission operator is described by

$$\mathcal{S}_{\boldsymbol{n}_1,m}^{\widetilde{1,\epsilon}} = \frac{i\rho\omega^2}{\widetilde{\delta}} \begin{pmatrix} \xi_p^{\widetilde{\epsilon}} & \frac{m}{\mathrm{R}}(\xi_p^{\widetilde{\epsilon}} \xi_s^{\widetilde{\epsilon}} - 2\frac{\widetilde{\delta}}{\kappa_s^2}) \\ -\frac{m}{\mathrm{R}}(\xi_p^{\widetilde{\epsilon}} \xi_s^{\widetilde{\epsilon}} - 2\frac{\widetilde{\delta}}{\kappa_s^2}) & \xi_s^{\widetilde{\epsilon}} \end{pmatrix}, \tag{93}$$

with $\xi_{\{p,s\}}^{\widetilde{\epsilon}} = \dfrac{1}{\kappa_{\{p,s\},\epsilon}} \displaystyle\sum_{\ell=0}^{L-1} \frac{R_\ell^\alpha}{S_\ell^\alpha - m^2/(\kappa_{\{p,s\},\epsilon}\mathrm{R})^2}$ and $\widetilde{\delta} = 1 + \dfrac{m^2}{\mathrm{R}^2} \xi_p^{\widetilde{\epsilon}} \xi_s^{\widetilde{\epsilon}}$. In the following, the angle of rotation is taken equal to $\alpha = \pi/4$, which was found to be optimal choice through numerical experiments in [28]. We report in Fig. 7 the spectral radius of $\mathcal{A}_m$ associated with the HO-TBC before and after a localization for different Padé orders, and in Fig. 8 the corresponding eigenvalue distributions of $(\mathcal{I} - \mathcal{A})$. The eigenvalues related to both the propagative and grazing modes are well approximated for the different Padé orders L. Increasing the Padé order leads to a better approximation of eigenvalues for evanescent modes (see Fig. 7) and hence of the spectral radius.

5. Finite element formulation

We describe in this section the implementation of the domain decomposition algorithm to solve the truncated Navier problem (3). Let us recall that the iterative method consists in solving problems (7) and computing the transmitted quantities (8). For the sake of clarity, we omit the index (p) associated to the iteration number of the algorithm.

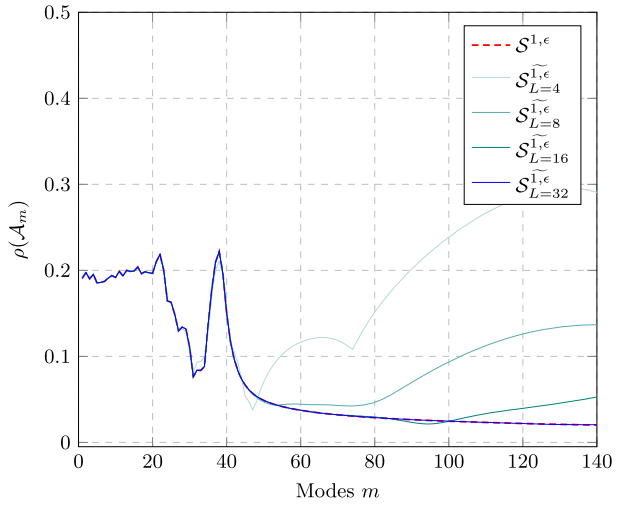


Fig. 7. Impact of the Padé localization of order L. Spectral radius of the modal iteration matrix $\mathcal{A}_m$ with respect to the mode m. $f = 6\,\text{Hz}$, $\text{R} = 1\,\text{m}$, $\lceil \kappa_p \rceil = 22\,\text{m}^{-1}$, $\lceil \kappa_s \rceil = 38\,\text{m}^{-1}$.

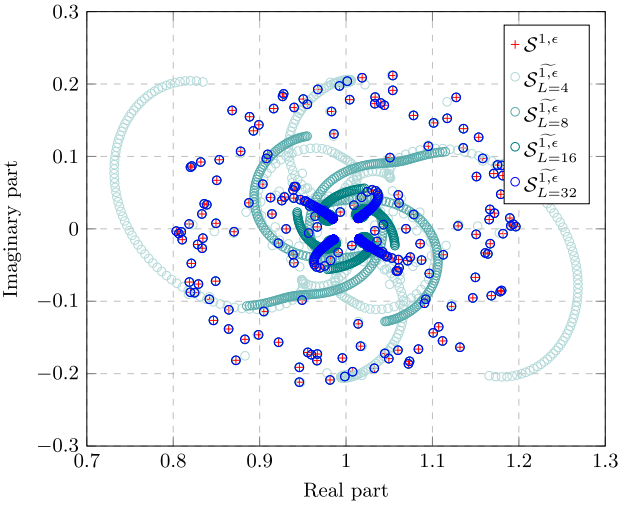


Fig. 8. Eigenvalues of $(\mathcal{I} - \mathcal{A})$ in the complex plane for the different transmission operators. $f = 6\,\text{Hz}$, $\text{R} = 1\,\text{m}$, $\lceil \kappa_p \rceil = 22\,\text{m}^{-1}$, $\lceil \kappa_s \rceil = 38\,\text{m}^{-1}$, $m^{\max} = 4\lfloor \kappa_s \rfloor$. (For interpretation of the colors in the figure(s), the reader is referred to the web version of this article.)

Weak formulation. Let us denote $\boldsymbol{u}_{g_i} \in (H^1(\Omega_i))^2$ such that $\boldsymbol{u}_{g_{i|\Gamma_i}} = \boldsymbol{u}_i^{\text{inc}}$ and $(H^1_g(\Omega_i))^2 := \left\{ \boldsymbol{u}_i \in (H^1(\Omega_i))^2 : \boldsymbol{u}_i = \boldsymbol{u}_{g_i} \text{ on } \Gamma_i \right\}$. In the case $\Gamma_i = \emptyset$, we have $(H^1_g(\Omega_i))^2 = (H^1(\Omega_i))^2$. Considering a test-function $\boldsymbol{u}'_i \in (H^1_0(\Omega_i))^2$, we get the variational formulation for the volume problem: find $\boldsymbol{u}_i \in (H^1_g(\Omega_i))^2$ such that

$$\int_{\Omega_i} (\sigma(\boldsymbol{u}_i) : \varepsilon(\boldsymbol{u}'_i) - \rho\omega^2 \boldsymbol{u}_i \cdot \boldsymbol{u}'_i) d\boldsymbol{x} - \int_{\Gamma_i^\infty} \mathcal{B}\boldsymbol{u}_i \cdot \boldsymbol{u}'_i d\Gamma_i^\infty - \sum_j \int_{\Sigma_{ij}} (\mathcal{S}_{\boldsymbol{n}_i} \boldsymbol{u}_i \cdot \boldsymbol{u}'_i + \boldsymbol{g}_{ij} \cdot \boldsymbol{u}'_i) d\Sigma_{ij} = 0, \tag{94}$$

holds for all $\boldsymbol{u}'_i$. Then, the variational formulation for the surface update (8) consists in finding $\boldsymbol{g}_{ji} \in (H^1(\Sigma_{ij}))^2$ such that

$$\int_{\Sigma_{ij}} (\boldsymbol{g}_{ji} \cdot \boldsymbol{g}'_{ji} + \boldsymbol{g}_{ij} \cdot \boldsymbol{g}'_{ij} + (\mathcal{S}_{\boldsymbol{n}_i} + \mathcal{S}_{\boldsymbol{n}_j}) \boldsymbol{u}_i \cdot \boldsymbol{g}'_{ji}) \, d\Sigma_{ij} = 0, \tag{95}$$

for all $\boldsymbol{g}'_{ji} \in (H^1_0(\Sigma_{ij}))^2$. For more details on the term $\int_{\Gamma_i^\infty} \mathcal{B}\boldsymbol{u}_i \cdot \boldsymbol{u}'_i d\Gamma_i^\infty$ we refer to [28] where the Lysmer-Kuhlemeyer Absorbing Boundary Condition (ABC) and high-order ABC have been addressed for 2D elasticity. We now compare two transmission boundary conditions on Σ_{ij}: the LO condition with $\mathcal{S}_{\boldsymbol{n}} = \mathcal{S}^0$ (13) and the Padé-local HO operator which is

defined by $\mathcal{S}_{\boldsymbol{n}} = \mathcal{S}_{\boldsymbol{n}}^{\widetilde{1,\epsilon}}$ (89). Let us explicit the terms $\int_{\Sigma_{ij}} \mathcal{S}_{\boldsymbol{n}_i} \boldsymbol{u}_i \cdot \boldsymbol{u}_i' d\Sigma_{ij}$ and $\int_{\Sigma_{ij}} (\mathcal{S}_{\boldsymbol{n}_i} + \mathcal{S}_{\boldsymbol{n}_j}) \boldsymbol{u}_i \cdot \boldsymbol{g}_{ji}' d\Sigma_{ij}$ in each case. We use the following notation for the standard scalar product on Σ_{ij}

$$(\boldsymbol{u}, \boldsymbol{u}') := \int_{\Sigma_{ij}} \boldsymbol{u} \cdot \boldsymbol{u}' d\Sigma_{ij}. \tag{96}$$

• *LO-TBC.*

$$\begin{aligned} (\mathcal{S}^0 \boldsymbol{u}_i, \boldsymbol{u}_i') &= i(\lambda + 2\mu)\kappa_p (\boldsymbol{n} \cdot \boldsymbol{u}_i, \boldsymbol{n} \cdot \boldsymbol{u}_i') + i\mu\kappa_s (\boldsymbol{\tau} \cdot \boldsymbol{u}_i, \boldsymbol{\tau} \cdot \boldsymbol{u}_i'), \\ \left((\mathcal{S}_{\boldsymbol{n}_i}^0 + \mathcal{S}_{\boldsymbol{n}_j}^0)\boldsymbol{u}_i, \boldsymbol{g}_{ji}'\right) &= (2\mathcal{S}^0 \boldsymbol{u}_i, \boldsymbol{g}_{ji}'). \end{aligned} \tag{97}$$

• *HO-TBC.*

$$(\mathcal{S}_{\boldsymbol{n}_i}^{\widetilde{1,\epsilon}} \boldsymbol{u}_i, \boldsymbol{u}_i') = ((\mathrm{I} + \Lambda_{\widetilde{2,\epsilon},\boldsymbol{n}_i})^{-1} \Lambda_{\widetilde{1,\epsilon}} \boldsymbol{u}_i, \boldsymbol{u}_i') + 2\mu(\mathcal{M}_{\boldsymbol{n}_i} \boldsymbol{u}_i, \boldsymbol{u}_i'). \tag{98}$$

Recall that the operators $\Lambda_{\widetilde{1,\epsilon}}$, $\Lambda_{\widetilde{2,\epsilon},\boldsymbol{n}_i}$ are given by the expressions (90) and (91) respectively. The variational formulation (98) is decomposed into three steps. For the sake of clarity, we omit in the following the index i relative to the sub-domain Ω_i for the several auxiliary variables we will introduce.

Step 1: The coupled variational formulation for the application of the operator $\Lambda_{\widetilde{1,\epsilon}}$ is given by: find $\boldsymbol{v}_i (:= \Lambda_{\widetilde{1,\epsilon}} \boldsymbol{u}_i)$ and the auxiliary scalar variables v_0, v_1, h_ℓ, i_ℓ, $\ell = 0, \ldots, L-1$ such that

$$\begin{cases} (\boldsymbol{v}_i, \boldsymbol{v}_i') = i\rho\omega^2 (\kappa_{p,\epsilon}^{-1}(v_0, \boldsymbol{n} \cdot \boldsymbol{v}_i') + \kappa_{s,\epsilon}^{-1}(v_1, \boldsymbol{\tau} \cdot \boldsymbol{v}_i')), \\ (v_0, v_0') = \displaystyle\sum_{\ell=0}^{L-1} R_\ell^\alpha (h_\ell, v_0'), \\ S_\ell^\alpha (h_\ell, h_\ell') - (\kappa_{p,\epsilon}^{-1} \partial_s h_\ell, \kappa_{p,\epsilon}^{-1} \partial_s h_\ell') = (\boldsymbol{n} \cdot \boldsymbol{u}_i, h_\ell'), \quad \ell = 0, \ldots, L-1, \\ (v_1, v_1') = \displaystyle\sum_{\ell=0}^{L-1} R_\ell^\alpha (i_\ell, v_1'), \\ S_\ell^\alpha (i_\ell, i_\ell') - (\kappa_{s,\epsilon}^{-1} \partial_s i_\ell, \kappa_{s,\epsilon}^{-1} \partial_s i_\ell') = (\boldsymbol{\tau} \cdot \boldsymbol{u}_i, i_\ell'), \quad \ell = 0, \ldots, L-1, \end{cases} \tag{99}$$

holds for all the associated test-functions $\boldsymbol{v}_i', v_0', v_1', h_\ell', i_\ell'$, $\ell = 0, \ldots, L-1$.

Step 2: The coupled variational formulation of the boundary differential equation $(\mathrm{I} + \Lambda_{\widetilde{2,\epsilon},\boldsymbol{n}_i})\boldsymbol{q}_i = \boldsymbol{v}_i$ on Σ_{ij}, with $\boldsymbol{v}_i = \Lambda_{\widetilde{1,\epsilon}} \boldsymbol{u}_i$ obtained at the Step 1, is expressed by: find $\boldsymbol{q}_i$ and the auxiliary scalar variables q_0, q_1, j_ℓ, k_ℓ, $\ell = 0, \ldots, L-1$ such that

$$\begin{cases} (\boldsymbol{q}_i, \boldsymbol{q}_i') - i(\kappa_{s,\epsilon}^{-1}(\partial_s q_0, \boldsymbol{\tau} \cdot \boldsymbol{q}_i') - \kappa_{p,\epsilon}^{-1}\left(\partial_s q_1, \boldsymbol{n} \cdot \boldsymbol{q}_i'\right)) = (\boldsymbol{v}_i, \boldsymbol{q}_i'), \\ (q_0, q_0') = \displaystyle\sum_{\ell=0}^{L-1} R_\ell^\alpha (j_\ell, q_0'), \\ S_\ell^\alpha (j_\ell, j_\ell') - (\kappa_{s,\epsilon}^{-1} \partial_s j_\ell, \kappa_{s,\epsilon}^{-1} \partial_s j_\ell') = (\boldsymbol{n} \cdot \boldsymbol{q}_i, j_\ell'), \quad \ell = 0, \ldots, L-1, \\ (q_1, q_1') = \displaystyle\sum_{\ell=0}^{L-1} R_\ell^\alpha (k_\ell, q_1'), \\ S_\ell^\alpha (k_\ell, k_\ell') - (\kappa_{p,\epsilon}^{-1} \partial_s k_\ell, \kappa_{p,\epsilon}^{-1} \partial_s k_\ell') = (\boldsymbol{\tau} \cdot \boldsymbol{q}_i, k_\ell'), \quad \ell = 0, \ldots, L-1, \end{cases} \tag{100}$$

holds for the associated test-functions $\boldsymbol{q}_i', q_0', q_1', j_\ell', k_\ell'$, $\ell = 0, \ldots, L-1$.

Step 3: The final step consists in finding an approximation $\boldsymbol{t}_i$ of the Neumann trace on Σ_{ij} such that

$$(\boldsymbol{t}_i, \boldsymbol{u}_i') = (\boldsymbol{q}_i, \boldsymbol{u}_i') + 2\mu(\mathcal{M}_{\boldsymbol{n}_i} \boldsymbol{u}_i, \boldsymbol{u}_i'), \tag{101}$$

where $\boldsymbol{q}_i$ is computed in Step 2 and $\mathcal{M}_{\boldsymbol{n}_i}$ is the tangential Günter derivative (18).

Using the properties of the operators given in Section 2.2 and the definition of $\boldsymbol{v}_i$ and $\boldsymbol{q}_i$, the term $\int_{\Sigma_{ij}} (\mathcal{S}_{\boldsymbol{n}_i} + \mathcal{S}_{\boldsymbol{n}_j}) \boldsymbol{u}_i \cdot \boldsymbol{g}_{ji}' d\Sigma_{ij}$ is finally described by

$$\left((\mathcal{S}_{\boldsymbol{n}_i} + \mathcal{S}_{\boldsymbol{n}_j})\boldsymbol{u}_i, \boldsymbol{g}_{ji}'\right) = (\boldsymbol{q}_i, \boldsymbol{g}_{ji}') + \left((I - \Lambda_{\widetilde{2,\epsilon},\boldsymbol{n}_i})^{-1} \boldsymbol{v}_i, \boldsymbol{g}_{ji}'\right). \tag{102}$$

We refer to Step 2 to produce $\left((I - \Lambda_{\widetilde{2,\epsilon},\boldsymbol{n}_i})^{-1} \boldsymbol{v}_i, \boldsymbol{g}_{ji}'\right)$.

Table 1
Physical parameters and number of degrees of freedom (d.o.f.). Mesh density $n_{\lambda_s} = 32$, Padé order $L = 4$, 2 sub-domains, "circle-concentric" partition, $\mathbb{P}_1$ finite elements.

f (Hz)	1			6		
λ_s (m)	1			1/6		
κ_s (rad m^{-1})	2π			12π		
d.o.f Mono-domain	37 376			994 230		
DDM System	Vol_1	Vol_2	Sur_{12}	Vol_1	Vol_2	Sur_{12}
d.o.f. LO-TBC	12 984	25 032	640	461 616	536 430	3 816
d.o.f. HO-TBC	21 304	33 352	4 480	511 224	586 038	26 712

Table 2
Important parameters of the HO-TBC and corresponding values used in all finite element computations.

Parameters	ϵ_s	ϵ_p	L	α
Values	$0.39\kappa_s^{1/3}(\mathcal{H}^2)^{1/3}$	$0.39\kappa_p^{1/3}(\mathcal{H}^2)^{1/3}$	4	$\pi/4$

Finite element discretization. Consider a covering $\Omega_{i,h}$ of Ω_i using $N_{i,T}$ triangular finite elements with $N_{i,V}$ vertices. Let us denote $\Gamma_{i,h}$ and $\Sigma_{ij,h}$ the boundaries of the mesh $\Omega_{i,h}$ corresponding to Γ_i and Σ_{ij} respectively. Parameter h is the average length of the edges of the triangles. For the discretization, we use classical $\mathbb{P}_1$ finite elements. We denote by $N_{i,\mathbb{P}_1}$ the vertices associated to the $\mathbb{P}_1$ finite elements and by $n_{\lambda_s} = \lambda_s/h$ the density of discretization points per S-wavelength. We consider three approximation spaces

$$\begin{cases} \mathbf{U}_{i,h} & := \{\boldsymbol{u}_{i,h} \in (\mathcal{C}^0(\Omega_i))^2 : \boldsymbol{u}_{i,h|T} \in (\mathbb{P}_1)^2, \forall T \in \Omega_{i,h}\} := (\mathbb{P}_1(\Omega_{i,h}))^2, \\ \mathbf{U}_{i,gh} & := \{\boldsymbol{u}_{i,h} \in \mathbf{U}_{i,h} : \boldsymbol{u}_{i,h} = \boldsymbol{u}_{i,h}^{\text{inc}} \text{ on } \Gamma_{i,h}\}, \\ \mathbf{V}_{i,h} & := \{\boldsymbol{v}_{i,h} \in (\mathcal{C}^0(\Sigma_{ij,h}))^2 : \boldsymbol{v}_{i,h|T} \in (\mathbb{P}_1)^2, \forall T \in \Sigma_{ij,h}\} := (\mathbb{P}_1(\Sigma_{ij,h}))^2, \end{cases} \tag{103}$$

with $\dim\mathbf{U}_{i,gh} = \dim\mathbf{U}_{i,h} = 2N_{i,\mathbb{P}_1}$ and $\dim\mathbf{V}_{i,h} = 2N_{i,b}$ where $N_{ij,b}$ is the number of boundary nodes on $\Sigma_{ij,h}$. Replacing in (97)-...-(102) $\boldsymbol{u}_i$ by $\boldsymbol{u}_{i,h} \in \mathbf{U}_{i,gh}$, $(\boldsymbol{v}_i, \boldsymbol{q}_i, \boldsymbol{t}_i)$ by $(\boldsymbol{v}_{i,h}, \boldsymbol{q}_{i,h}, \boldsymbol{t}_{i,h}) \in \mathbf{V}_{i,h}^3$, (v_0, v_1, q_0, q_1) by $(v_{0,h}, v_{1,h}, q_{0,h}, q_{1,h}) \in \mathbb{P}_1(\Sigma_{ij,h})^4$ and $\forall \ell = 0, \cdots, L-1$, $(h_\ell, i_\ell, j_\ell, k_\ell)$ by $(h_{\ell,h}, i_{\ell,h}, j_{\ell,h}, k_{\ell,h}) \in \mathbb{P}_1(\Sigma_{ij,h})^4$, we obtain the discretization of the weak formulations (94)–(95) for the low-order and high-order transmission boundary conditions.

Let us now discuss on the size of the linear systems involved in the DDM resolution. We recall that on sub-domain Ω_i, we solve the volume problem Vol_i corresponding to the weak formulation (94) and n surface problem(s) Sur_{ij} corresponding to (95), where n is the number of sub-domains neighboring the current sub-domain Ω_i. For instance, in a "circle-concentric" partition, Ω_i has one or two neighboring sub-domains, so $n = 1$ or 2. Considering the LO-TBC or the HO-TBC leads to different sizes of the volume and surface problems. Indeed, the DDM problem with the LO-TBC has no additional variables, in the sense that only $\boldsymbol{u}_i$ and $\boldsymbol{g}_{ji}$ have to be calculated, whereas with the HO-TBC, some auxiliary variables (that are $\boldsymbol{v}_i, \boldsymbol{q}_i, \boldsymbol{t}_i, v_0, v_1, q_0, q_1, h_\ell, i_\ell, j_\ell, k_\ell$) are also needed. With the LO-TBC, the resolution of Vol_i leads to a linear system of size $2N_{i,\mathbb{P}_1}$ and Sur_{ij} to a linear system of size $2N_{i,b}$. For the implementation of the HO-TBC, Steps 1, 2 and (102) require each $(2L+4)$ additional variables on Σ_{ij}. The resolution of Vol_i leads to a linear system of size $2N_{i,\mathbb{P}_1} + 2(2L+4)N_{i,b} + 2N_{i,b}$ and Sur_{ij} to a linear system of size $2N_{i,b} + (2L+4)N_{i,b}$. Note that $N_{i,b} \ll N_{i,\mathbb{P}_1}$.

6. Numerical results

In this section, we validate numerically the new domain-decomposition algorithm using the HO-TBC and compare it with the LO-TBC. We study the scattering of incident elastic plane waves by the unit disk. The fictitious boundary Γ^∞ is the circle of radius $r_{\text{ext}} = 2$ m. The truncated computational domain is the annular domain bounded by the unit circle and $\Gamma^\infty := C_{r_{\text{ext}}}$. We fix again the relation $\kappa_s = \sqrt{3}\kappa_p$. In the following, the frequencies $f = 1$ Hz and $f = 6$ Hz are mainly used. We denote by n_{λ_s} the density of discretization points per S-wavelength $\lambda_s = 2\pi/\kappa_s$. We recap some physical parameters and number of degrees of freedom in Table 1. We consider unstructured meshes which are generated using Gmsh [22]. The simulations are performed with the open source finite element solver GetDP [15,21]. All the tests are run on a Intel Core i5-6300U (with two CPU cores 2.40 GHz). The efficiency and accuracy of the HO-TBC (89) depend on different parameters: the damping parameters $\epsilon_{\{p,s\}}$, the order $2L+1$ and the angle α of the Padé approximation. We summarize the parameters used for all the following simulations (unless indicated otherwise) in Table 2. The choice of the regularizing parameters $\epsilon_{\{p,s\}}$ and the ones used in the localization process has been discussed in Sections 3 and 4. From now, the L2 error considered is

$$e_{L^2} := \frac{\|\boldsymbol{u}_{\text{FEM}} - \boldsymbol{u}_{\text{DDM}}\|_{L^2}}{\|\boldsymbol{u}_{\text{FEM}}\|_{L^2}}, \tag{104}$$

with $\boldsymbol{u}_{\text{FEM}}$ the FEM solution with $\mathbb{P}_1$ elements to (3) on the mono-domain and $\boldsymbol{u}_{\text{DDM}}$ the reconstruction of the scattered field on the global domain after a DDM computation solution to (7)–(8) with LO-TBC (13) or HO-TBC (89).

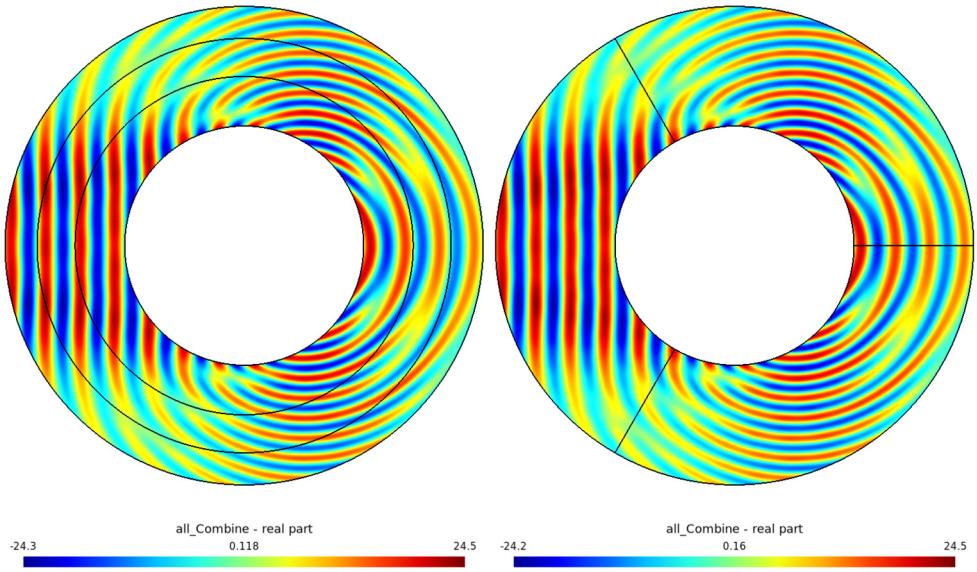


Fig. 9. Two-dimensional test cases: comparison between the DDM solution with a "circle-concentric"decomposition (left) and a "circle-pie" decomposition (right). First component $\mathrm{Re}(\boldsymbol{u}_x)$ of the solution. Incident P-wave, frequency $f = 6\,\mathrm{Hz}$, $\kappa_s = \sqrt{3}\kappa_p$, mesh density $n_{\lambda_s} = 32$, $N_{\mathrm{dom}} = 3$, $r_{\mathrm{ext}} = 2\,\mathrm{m}$, HO-TBC, HO-ABC, GMRES Tolerance$= 10^{-4}$, Padé order approximation $L = 4$, $\alpha = \pi/4$, $\mathbb{P}_1$ finite elements.

6.1. Impact of the partition of the domain

We consider in Fig. 9 incident plane P-waves $\boldsymbol{u}_p^{\mathrm{inc}}(\mathbf{x}) = (-i\kappa_p e^{-i\kappa_p x}, 0)^t$ striking the unit disk and HO-TBC (89) onto the fictitious boundaries splitting the domain. Both solutions are taken with the same mesh refinement $n_{\lambda_s} = 32$. The high-order ABC [28] is set on Γ^∞.

For the two decompositions, the DDM algorithm converges and gives the results in Fig. 9. For the "circle-concentric" configuration, we obtain $e_{L^2} = 8.95\text{e-}05$ with 17 GMRES iterations and for the "circle-pie" geometry $e_{L^2} = 1.48\text{e-}02$ with 103 iterations. This difference is mainly due to the way the domain is split. For the "circle-pie" case, there are intersections between the transmission boundaries and the boundaries Γ and Γ^∞, which introduces cross-points [20,29]. From now, let us consider the "circle-concentric" partition.

6.2. Influence of the frequency, the mesh density and the number of sub-domains

We consider $N_{\mathrm{dom}} = 2$ sub-domains. It is well-known that taking incident plane P- or S-waves (in practice $\boldsymbol{u}_p^{\mathrm{inc}}(\mathbf{x}) = (-i\kappa_p e^{-i\kappa_p x}, 0)^t$ respectively $\boldsymbol{u}_s^{\mathrm{inc}}(\mathbf{x}) = (0, i\kappa_s e^{-i\kappa_s x})^t$) and/or changing the frequency could impact the GMRES convergence. Fig. 10 depicts the number of iterations to reach convergence with respect to the frequency f and the incident plane wave for a fixed density of discretization points per wavelength $n_{\lambda_s} = 32$. The HO-TBC is very efficient. The number of iterations are reduced compared with the LO-TBC, particularly for high frequencies and S-waves. The HO-TBC requires a number of iterations quasi-independent of the frequency. Fig. 11 gives the number of iterations with respect to the density of discretization n_{λ_s}, for a fixed frequency $f = 1\,\mathrm{Hz}$. The interest of using the HO-TBC is confirmed.

In Fig. 12, we observe the effect of the number of sub-domains on the GMRES iterations. We directly see that the different methods scale for the two TBCs. The HO-TBC leads to a faster GMRES convergence than the LO-TBC.

6.3. Influence of the ratio between the two wavenumbers

In this section, we observe the impact of the ratio between the two wavenumbers κ_s/κ_p onto the numbers of GMRES iterations. Let us first explicit κ_s/κ_p

$$\frac{\kappa_s}{\kappa_p} := \sqrt{\frac{\lambda + 2\mu}{\mu}}. \tag{105}$$

One can remark that the ratio (105) depends only on the Lamé coefficients. In order to get an interesting interval physically speaking, we consider three materials with different stiffness: steel (very rigid, $\lambda \simeq 104\,\mathrm{GPa}$ and $\mu \simeq 82\,\mathrm{GPa}$), aluminum (rigid, $\lambda \simeq 57\,\mathrm{GPa}$ and $\mu \simeq 25\,\mathrm{GPa}$) and cork (little stiff, $\lambda \simeq 10^{-3}\,\mathrm{GPa}$ and $\mu \simeq 9e^{-03}\,\mathrm{GPa}$). The corresponding ratio are $(\kappa_p/\kappa_s)_{\mathrm{steel}} \simeq 1.81$, $(\kappa_p/\kappa_s)_{\mathrm{aluminium}} \simeq 2.07$ and $(\kappa_p/\kappa_s)_{\mathrm{cork}} \simeq 1.45$. Thus, we choose to study κ_p/κ_s in $[\sqrt{2}, 3]$ (corresponding

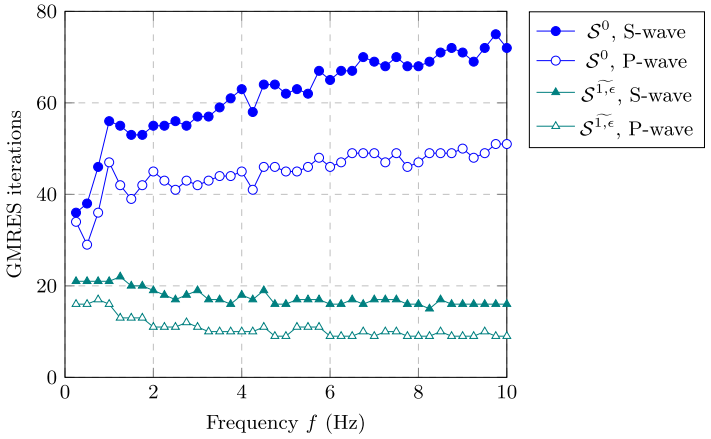


Fig. 10. Number of GMRES iterations vs. frequency. Comparison between the LO-TBC ($\mathcal{S}^0$) and the HO-TBC ($\mathcal{S}^{\widetilde{1,\epsilon}}$). Incident P-wave and S-wave. Frequency $0.25 \leq f \leq 10\,(\text{Hz})$, $\kappa_s = \sqrt{3}\kappa_p$. Mesh density $n_{\lambda_s} = 32$, $N_{\text{dom}} = 2$, "circle-concentric" partition, $r_{\text{ext}} = 2\,\text{m}$, HO-ABC, GMRES Tolerance$= 10^{-4}$, Padé order approximation $L = 4$, $\alpha = \pi/4$, $\mathbb{P}_1$ finite elements.

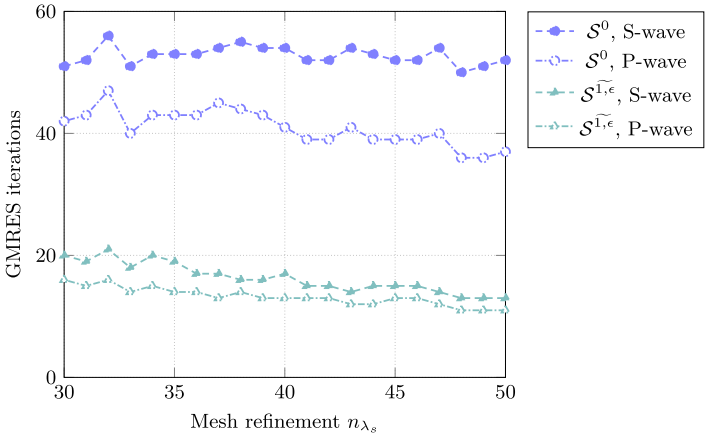


Fig. 11. Number of GMRES iterations vs. mesh density. Comparison between the LO-TBC ($\mathcal{S}^0$) and the HO-TBC ($\mathcal{S}^{\widetilde{1,\epsilon}}$). Incident P-wave and S-wave. Mesh density $30 \leq n_{\lambda_s} \leq 50$. Frequency $f = 1\,\text{Hz}$, $N_{\text{dom}} = 2$, $\kappa_s = \sqrt{3}\kappa_p$, "circle-concentric" partition, $r_{\text{ext}} = 2\,\text{m}$, HO-ABC, GMRES Tolerance$= 10^{-4}$, Padé order approximation $L = 4$, $\alpha = \pi/4$, $\mathbb{P}_1$ finite elements.

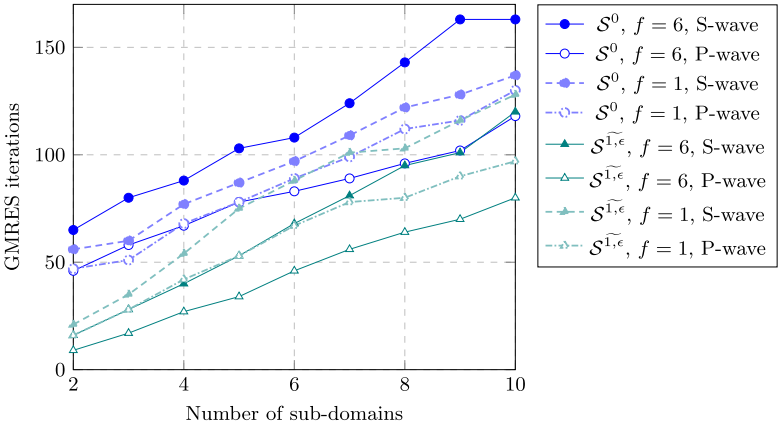


Fig. 12. Number of GMRES iterations vs. number of sub-domains. Comparison between the LO-TBC ($\mathcal{S}^0$) and the HO-TBC ($\mathcal{S}^{\widetilde{1,\epsilon}}$). Frequencies $f = 1\,\text{Hz}$ and $f = 6\,\text{Hz}$. Incident P-wave and S-wave. Mesh density $n_{\lambda_s} = 32$, $\kappa_s = \sqrt{3}\kappa_p$, "circle-concentric" partition, $r_{\text{ext}} = 2\,\text{m}$, HO-ABC, GMRES Tolerance$= 10^{-4}$, Padé order approximation $L = 4$, $\alpha = \pi/4$, $\mathbb{P}_1$ finite elements.

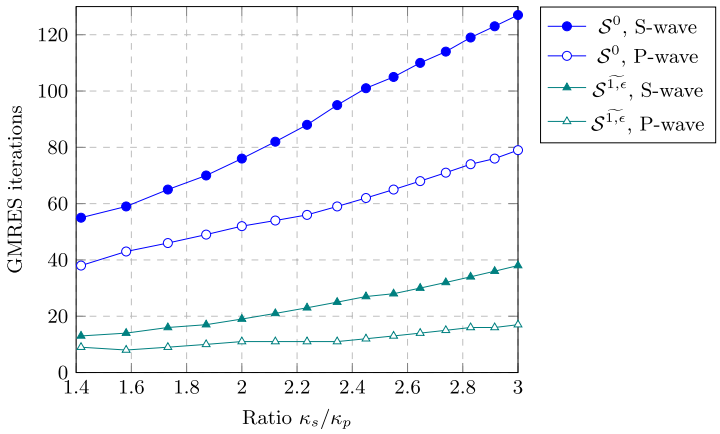


Fig. 13. Number of GMRES iterations vs. ratio of the wavenumbers. Comparison between the LO-TBC ($\mathcal{S}^0$) and the HO-TBC ($\mathcal{S}^{\widetilde{1,\epsilon}}$). Incident P-wave and S-wave. Mesh density $n_{\lambda_s} = 32$, $\kappa_s = 12\pi$ (m^{-1}), $N_{\mathrm{dom}} = 2$, "circle-concentric" partition, $r_{\mathrm{ext}} = 2\,\mathrm{m}$, HO-ABC, GMRES Tolerance$= 10^{-4}$, Padé order approximation $L = 4$, $\alpha = \pi/4$, $\mathbb{P}_1$ finite elements.

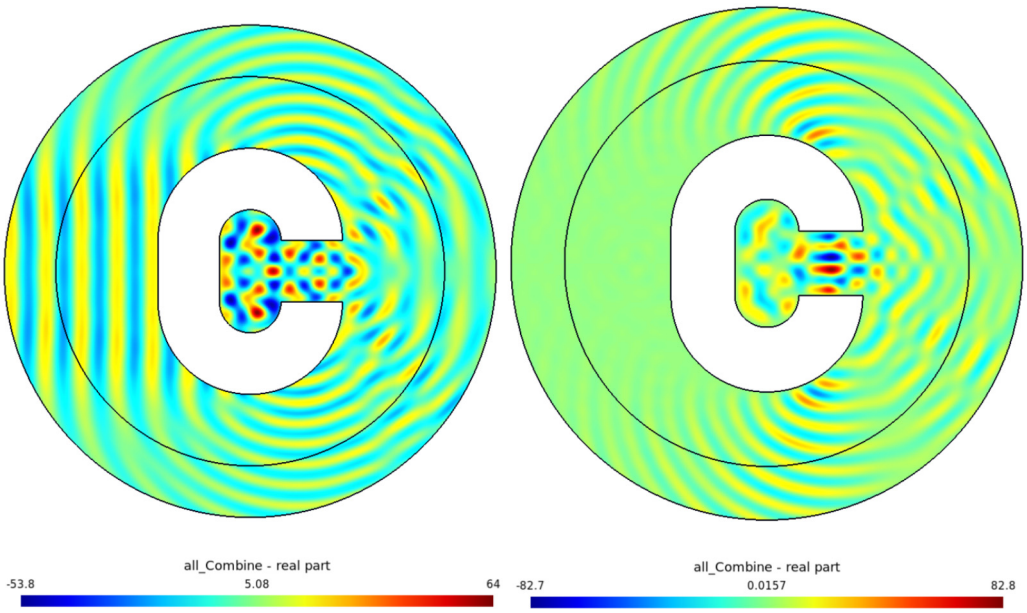


Fig. 14. Two-dimensional test cases with "letter C" scatterer. Incident P-wave (left) and S-wave (right). First component Re($\boldsymbol{u}_x$) of the solution. Frequency $f = 6\,\mathrm{Hz}$, $\kappa_s = \sqrt{3}\kappa_p$, mesh density $n_{\lambda_s} = 32$, $N_{\mathrm{dom}} = 2$, $r_{\mathrm{ext}} = 2\,\mathrm{m}$, HO-TBC, HO-ABC, GMRES Tolerance$= 10^{-4}$, Padé order approximation $L = 4$, $\alpha = \pi/4$, $\mathbb{P}_1$ finite elements.

respectively to $\lambda \ll \mu$ and $\lambda = 7\mu$). Results are reported in Fig. 13. The new high-order transmission conditions again outperform the low-order one.

6.4. Influence of the scatterer geometry

In this section, we consider another geometry for the scatterer: the letter "C". We include the letter "C" into the unit disk (which was the previous scatterer). This geometry generates multiple diffractions as shown in Fig. 14 where the DDM with HO-TBC for two subdomains had been performed. The test case with incident P-wave (left) is obtained after 9 GMRES iterations with an L^2 error of 5.69e-05 and for the incident S-wave (right) 15 GMRES iterations and $e_{L^2} = 5.87\text{e-}05$. In order to test the impact of the geometry onto the convergence of the algorithm, we take the same cases as in section 6.2 i.e. changing the frequency f and with incident P- or S-wave. We obtain the results reported in Fig. 15. We remark that we get a similar behavior as the disk scatterer (see Fig. 10). It also confirms the interest of using the HO-TBC.

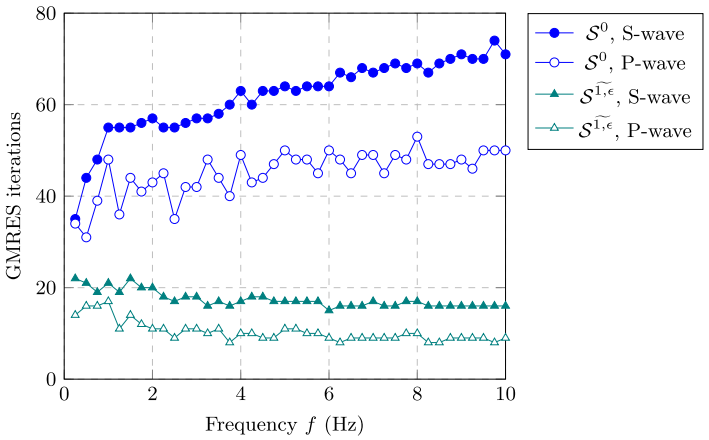


Fig. 15. Number of GMRES iterations vs. frequency. Comparison between the LO-TBC ($\mathcal{S}^0$) and the HO-TBC ($\mathcal{S}^{\widetilde{1,\epsilon}}$). Letter C scatterer. Incident P-wave and S-wave. Mesh density $n_{\lambda_s} = 32$, $N_{\text{dom}} = 2$, $\kappa_s = \sqrt{3}\kappa_p$, "circle-concentric" partition, $r_{\text{ext}} = 2\,\text{m}$, HO-ABC, GMRES Tolerance$= 10^{-4}$, Padé order approximation $L = 4$, $\alpha = \pi/4$, $\mathbb{P}_1$ finite elements.

7. Conclusion

We have proposed a first non overlapping domain decomposition method for the Navier equation in the two-dimensional, isotropic case. The method is based on the use of an approximate DtN map at the transmission interfaces between the sub-domains. A detailed asymptotic convergence analysis for a model problem with two sub-domains has been performed, showing the quasi-optimality of the method, i.e. an optimal convergence rate for large modes and an improved convergence rate for the other modes compared to the standard low-order method. Finally, numerical test cases were used to confirm the effectiveness of the proposed method for 2D finite element simulations. The extension of the method to three dimensions is currently under investigation.

Declaration of competing interest

The authors have no affiliation with any organization with a direct or indirect financial interest in the subject matter discussed in the manuscript

Acknowledgement

This research was funded in part through the ARC grant for Concerted Research Actions (ARC WAVES 15/19-03), financed by the Wallonia-Brussels Federation of Belgium.

Appendix A. The iteration matrix

In this section, we explicit the terms of the 4×4 iteration matrix $\mathcal{A}_m$ (59). Let us recall that

$$\mathcal{A}_m := \begin{pmatrix} \mathbf{0}_2 & \mathcal{A}_{0,m} \\ \mathcal{A}_{1,m} & \mathbf{0}_2 \end{pmatrix}, \tag{A.1}$$

with (see (58)–(57))

$$\mathcal{A}_{0,m} := \begin{pmatrix} A_{4,m} & A_{5,m} \\ A_{6,m} & A_{7,m} \end{pmatrix} \begin{pmatrix} A_{0,m} & A_{1,m} \\ A_{2,m} & A_{3,m} \end{pmatrix}^{-1}, \quad \mathcal{A}_{1,m} := \begin{pmatrix} B_{0,m} & B_{1,m} \\ B_{2,m} & B_{3,m} \end{pmatrix} \begin{pmatrix} B_{4,m} & B_{5,m} \\ B_{6,m} & B_{7,m} \end{pmatrix}^{-1}, \tag{A.2}$$

and $A_{j,m}$, $B_{j,m}$, for $j = 1, \cdots, 7$, given in section 3.3. We deduce

$$\mathcal{A}_{0,m} = \frac{1}{A_{0,m}A_{3,m} - A_{1,m}A_{2,m}} \begin{pmatrix} A_{3,m}A_{4,m} - A_{2,m}A_{5,m} & A_{0,m}A_{5,m} - A_{1,m}A_{4,m} \\ A_{3,m}A_{6,m} - A_{2,m}A_{7,m} & A_{0,m}A_{7,m} - A_{1,m}A_{6,m} \end{pmatrix}, \tag{A.3}$$

and

$$\mathcal{A}_{1,m} = \frac{1}{B_{4,m}B_{7,m} - B_{5,m}B_{6,m}} \begin{pmatrix} B_{0,m}B_{7,m} - B_{1,m}B_{6,m} & B_{1,m}B_{4,m} - B_{0,m}B_{5,m} \\ B_{2,m}B_{7,m} - B_{3,m}B_{6,m} & B_{3,m}B_{4,m} - B_{2,m}B_{5,m} \end{pmatrix}. \tag{A.4}$$

We are thus interested in finding the eight following coefficients

$$\begin{aligned} a_m &:= \frac{A_{3,m}A_{4,m} - A_{2,m}A_{5,m}}{A_{0,m}A_{3,m} - A_{1,m}A_{2,m}}, \quad & b_m &:= \frac{A_{0,m}A_{5,m} - A_{1,m}A_{4,m}}{A_{0,m}A_{3,m} - A_{1,m}A_{2,m}}, \\ c_m &:= \frac{A_{3,m}A_{6,m} - A_{2,m}A_{7,m}}{A_{0,m}A_{3,m} - A_{1,m}A_{2,m}}, \quad & d_m &:= \frac{A_{0,m}A_{7,m} - A_{1,m}A_{6,m}}{A_{0,m}A_{3,m} - A_{1,m}A_{2,m}}, \\ e_m &:= \frac{B_{0,m}B_{7,m} - B_{1,m}B_{6,m}}{B_{4,m}B_{7,m} - B_{5,m}B_{6,m}}, \quad & f_m &:= \frac{B_{1,m}B_{4,m} - B_{0,m}B_{5,m}}{B_{4,m}B_{7,m} - B_{5,m}B_{6,m}} \\ g_m &:= \frac{B_{2,m}B_{7,m} - B_{3,m}B_{6,m}}{B_{4,m}B_{7,m} - B_{5,m}B_{6,m}}, \quad & h_m &:= \frac{B_{3,m}B_{4,m} - B_{2,m}B_{5,m}}{B_{4,m}B_{7,m} - B_{5,m}B_{6,m}}, \end{aligned} \tag{A.5}$$

defining the iteration matrix

$$\mathcal{A}_m := \begin{pmatrix} 0 & 0 & a_m & b_m \\ 0 & 0 & c_m & d_m \\ e_m & f_m & 0 & 0 \\ g_m & h_m & 0 & 0 \end{pmatrix}. \tag{A.6}$$

Let us start with determining the denominators $A_{0,m}A_{3,m} - A_{1,m}A_{2,m}$ and $B_{4,m}B_{7,m} - B_{5,m}B_{6,m}$. For the sake of simplicity, we denote in the following $H_{\{p,s\}} = H_m(\kappa_{\{p,s\}}r)$, $H'_{\{p,s\}} = H'_m(\kappa_{\{p,s\}}r)$, $J_{\{p,s\}} = J_m(\kappa_{\{p,s\}}r)$ and $J'_{\{p,s\}} = J'_m(\kappa_{\{p,s\}}r)$. Simple calculations lead to

$$\begin{aligned} A_{0,m}A_{3,m} - A_{1,m}A_{2,m} &= b_0 H_s H_p + b_1 H_s H'_p + b_2 H'_s H_p + b_3 H'_s H'_p, \\ B_{4,m}B_{7,m} - B_{5,m}B_{6,m} &= b_4 J_p J_s + b_5 J'_p J_s + b_6 J_p J'_s + b_7 J'_p J'_s, \end{aligned} \tag{A.7}$$

while considering

$$\begin{cases} b_0 = -\dfrac{\rho^2\omega^4}{\delta} - 2i\mu\dfrac{\rho\omega^2}{\delta}\dfrac{m^2}{r^3}(\xi_p^\epsilon + \xi_s^\epsilon) + 4\mu^2\dfrac{m^2}{r^4}, \\ b_1 = \rho\omega^2\kappa_p\left(\dfrac{i\rho\omega^2\xi_p^\epsilon}{\delta} - \dfrac{2\mu}{r}\right), \\ b_2 = \rho\omega^2\kappa_s\left(\dfrac{i\rho\omega^2\xi_s^\epsilon}{\delta} - \dfrac{2\mu}{r}\right), \\ b_3 = \kappa_p\kappa_s\left(\dfrac{\rho^2\omega^4}{\delta}\xi_p^\epsilon\xi_s^\epsilon + \dfrac{2i\mu}{r}\dfrac{\rho\omega^2}{\delta}(\xi_p^\epsilon + \xi_s^\epsilon) - \dfrac{4\mu^2}{\mathrm{R}^2}\right), \\ b_4 = -\dfrac{\rho^2\omega^4}{\delta} + 2i\mu\dfrac{\rho\omega^2}{\delta}\dfrac{m^2}{r^3}(\xi_p^\epsilon + \xi_s^\epsilon) + 4\mu^2\dfrac{m^2}{r^4}, \\ b_5 = -\rho\omega^2\kappa_p\left(\dfrac{i\rho\omega^2\xi_p^\epsilon}{\delta} + \dfrac{2\mu}{r}\right), \\ b_6 = -\rho\omega^2\kappa_s\left(\dfrac{i\rho\omega^2\xi_s^\epsilon}{\delta} + \dfrac{2\mu}{r}\right), \\ b_7 = \kappa_p\kappa_s\left(\dfrac{\rho^2\omega^4}{\delta}\xi_p^\epsilon\xi_s^\epsilon - \dfrac{2i\mu}{r}\dfrac{\rho\omega^2}{\delta}(\xi_p^\epsilon + \xi_s^\epsilon) - \dfrac{4\mu^2}{\mathrm{R}^2}\right). \end{cases} \tag{A.8}$$

The numerators of $a_m, b_m, c_m, d_m, e_m, f_m, g_m, h_m$ are given by

$$\begin{cases} A_{3,m}A_{4,m} - A_{2,m}A_{5,m} = c_0 H_p H_s + c_1 H'_p H_s + c_2 H_p H'_s + c_3 H'_p H'_s, \\ A_{0,m}A_{5,m} - A_{1,m}A_{4,m} = \dfrac{2m}{r}\dfrac{\rho^2\omega^4}{\delta^2}\xi_p^\epsilon\left(H_p H_s + \xi_p^\epsilon\xi_s^\epsilon\kappa_p\kappa_s H'_p H'_s\right), \\ A_{3,m}A_{6,m} - A_{2,m}A_{7,m} = -\dfrac{2m}{r}\dfrac{\rho^2\omega^4}{\delta^2}\xi_s^\epsilon\left(H_p H_s + \xi_p^\epsilon\xi_s^\epsilon\kappa_p\kappa_s H'_p H'_s\right), \\ A_{0,m}A_{7,m} - A_{1,m}A_{6,m} = c_4 H_p H_s + c_5 H'_p H_s + c_6 H_p H'_s + c_7 H'_p H'_s, \end{cases} \tag{A.9}$$

and

$$\begin{cases} B_{0,m}B_{7,m} - B_{1,m}B_{6,m} &= c_4 J_p J_s + c_5 J'_p J_s + c_6 J_p J'_s + c_7 J'_p J'_s, \\ B_{1,m}B_{4,m} - B_{0,m}B_{5,m} &= -\dfrac{2m}{r}\dfrac{\rho^2\omega^4}{\delta^2}\xi_p^\epsilon \left(J_p J_s + \xi_p^\epsilon \xi_s^\epsilon \kappa_p \kappa_s J'_p J'_s\right), \\ B_{2,m}B_{7,m} - B_{3,m}B_{6,m} &= \dfrac{2m}{r}\dfrac{\rho^2\omega^4}{\delta^2}\xi_s^\epsilon \left(J_p J_s + \xi_p^\epsilon \xi_s^\epsilon \kappa_p \kappa_s J'_p J'_s\right), \\ B_{3,m}B_{4,m} - B_{2,m}B_{5,m} &= c_0 J_p J_s + c_1 J'_p J_s + c_2 J_p J'_s + c_3 J'_p J'_s, \end{cases} \tag{A.10}$$

with

$$\begin{cases} c_0 &= \dfrac{\rho^2\omega^4}{\delta^2}\left(1 - \dfrac{m^2}{\mathrm{R}^2}\xi_p^\epsilon \xi_s^\epsilon\right) + 2i\mu\dfrac{\rho\omega^2}{\delta}\dfrac{m^2}{r^3}(\xi_s^\epsilon - \xi_p^\epsilon) - 4\mu^2\dfrac{m^2}{r^4}, \\ c_1 &= \rho\omega^2\kappa_p\left(\dfrac{i\rho\omega^2\xi_p^\epsilon}{\delta} + \dfrac{2\mu}{r}\right), \\ c_2 &= \rho\omega^2\kappa_s\left(-\dfrac{i\rho\omega^2\xi_s^\epsilon}{\delta} + \dfrac{2\mu}{r}\right), \\ c_3 &= \kappa_p\kappa_s\left(\dfrac{\rho^2\omega^4}{\delta^2}\xi_p^\epsilon\xi_s^\epsilon\left(1 - \dfrac{m^2}{\mathrm{R}^2}\xi_p^\epsilon\xi_s^\epsilon\right) - \dfrac{2i\mu}{r}\dfrac{\rho\omega^2}{\delta}(\xi_s^\epsilon - \xi_p^\epsilon) + \dfrac{4\mu^2}{\mathrm{R}^2}\right), \\ c_4 &= \dfrac{\rho^2\omega^4}{\delta^2}\left(1 - \dfrac{m^2}{\mathrm{R}^2}\xi_p^\epsilon \xi_s^\epsilon\right) - 2i\mu\dfrac{\rho\omega^2}{\delta}\dfrac{m^2}{r^3}(\xi_s^\epsilon - \xi_p^\epsilon) - 4\mu^2\dfrac{m^2}{r^4}, \\ c_5 &= \rho\omega^2\kappa_p\left(-\dfrac{i\rho\omega^2\xi_p^\epsilon}{\delta} + \dfrac{2\mu}{r}\right), \\ c_6 &= \rho\omega^2\kappa_s\left(\dfrac{i\rho\omega^2\xi_s^\epsilon}{\delta} + \dfrac{2\mu}{r}\right), \\ c_7 &= \kappa_p\kappa_s\left(\dfrac{\rho^2\omega^4}{\delta^2}\xi_p^\epsilon\xi_s^\epsilon\left(1 - \dfrac{m^2}{\mathrm{R}^2}\xi_p^\epsilon\xi_s^\epsilon\right) + \dfrac{2i\mu}{r}\dfrac{\rho\omega^2}{\delta}(\xi_s^\epsilon - \xi_p^\epsilon) + \dfrac{4\mu^2}{\mathrm{R}^2}\right). \end{cases} \tag{A.11}$$

References

[1] M. Abramowitz, I.A. Stegun, Handbook of Mathematical Functions with Formulas, Graphs, and Mathematical Tables, 1974.
[2] X. Antoine, M. Darbas, Y.Y. Lu, An improved surface radiation condition for high-frequency acoustic scattering problems, Comput. Methods Appl. Mech. Eng. 195 (33–36) (2006) 4060–4074.
[3] A. Bendali, Y. Boubendir, M'B. Fares, A feti-like domain decomposition method for coupling fem and bem in large-size problems of acoustic scattering, Comput. Struct. 85 (2007) 526–535.
[4] J.P. Berenger, A perfectly matched layer for the absorption of electromagnetic waves, J. Comput. Phys. 114 (2) (1994) 185–200.
[5] M. El Bouajaji, B. Thierry, X. Antoine, C. Geuzaine, A quasi-optimal domain decomposition algorithm for the time-harmonic maxwell's equations, J. Comput. Phys. 294 (2015) 38–57.
[6] Y. Boubendir, X. Antoine, C. Geuzaine, A quasi-optimal non-overlapping domain decomposition algorithm for the Helmholtz equation, J. Comput. Phys. 231 (2) (2012) 262–280.
[7] R. Brunet, V. Dolean, M.J. Gander, Natural domain decomposition algorithms for the solution of time-harmonic elastic waves, Preprint https://arxiv.org/abs/1904.12158, Apr 2019.
[8] S. Chaillat, M. Darbas, F. Le Louër, Approximate local Dirichlet-to-Neumann map for three-dimensional time-harmonic elastic waves, Comput. Methods Appl. Mech. Eng. 297 (2015) 62–83.
[9] S. Chaillat, M. Darbas, F. Le Louër, Fast iterative boundary element methods for high-frequency scattering problems in 3D elastodynamics, J. Comput. Phys. 341 (2017) 429–446.
[10] W.C. Chew, Q.H. Liu, Perfectly matched layers for elastodynamics: a new absorbing boundary condition, J. Comput. Acoust. 04 (04) (1996) 341–359.
[11] M. Darbas, Préconditionneurs analytiques de type Calderón pour les formulations intégrales des problèmes de diffraction d'ondes, PhD Thesis INSA, Toulouse, 2004.
[12] M. Darbas, F. Le Louër, Well-conditioned boundary integral formulations for the iterative solution of elastic scattering problems, Math. Methods Appl. Sci. 38 (2015) 1705–1733.
[13] B. Després, Méthodes de décomposition de domaine pour la propagation d'ondes en régime harmonique. Le théorème de Borg pour l'équation de Hill vectorielle, 1991, 1991PA090032, PhD Thesis.
[14] V. Dolean, P. Jolivet, F. Nataf, An Introduction to Domain Decomposition Methods, Algorithms, Theory, and Parallel Implementation, 2015.
[15] P. Dular, C. Geuzaine, F. Henrotte, W. Legros, A general environment for the treatment of discrete problems and its application to the finite element method, IEEE Trans. Magn. 34 (5) (1998) 3395–3398.
[16] M. El Bouajaji, X. Antoine, C. Geuzaine, Approximate local magnetic-to-electric surface operators for time-harmonic maxwell's equations, J. Comput. Phys. 279 (2014) 241–260.
[17] O.G. Ernst, M.J. Gander, Why it is difficult to solve Helmholtz problems with classical iterative methods, in: Numerical Analysis of Multiscale Problems, Springer, 2012, pp. 325–363.
[18] Y.C. Fung, Pin Tong, Classical and Computational Solid Mechanics, World Scientific, 2001.
[19] Günter K. Gächter, Marcus J. Grote, Dirichlet-to-Neumann map for three-dimensional elastic waves, Wave Motion 37 (3) (2003) 293–311.
[20] M.J. Gander, K. Santugini-Repiquet, Cross-points in domain decomposition methods with a finite element discretization, Electron. Trans. Numer. Anal. 45 (2014) 219–240.

[21] C. Geuzaine, GetDP: a general finite-element solver for the de Rham complex, PAMM 7 (2008).
[22] C. Geuzaine, J.-F. Remacle, Gmsh: a 3-D finite element mesh generator with built-in pre- and post-processing facilities, Int. J. Numer. Methods Eng. 79 (11) (2009) 1309–1331.
[23] D. Givoli, J.B. Keller, Non-reflecting boundary conditions for elastic waves, Wave Motion 12 (1990) 261–279.
[24] M. Grote, J. Keller, Exact nonreflecting boundary condition for elastic waves, SIAM I. Appl. Math. 60 (2000) 803–819.
[25] V.D. Kupradze, T.G. Gegelia, M.O. Basheleĭshvili, T.V. Burchuladze, Three-dimensional problems of the mathematical theory of elasticity and thermoelasticity, in: V.D. Kupradze (Ed.), Russian edition, in: North-Holland Series in Applied Mathematics and Mechanics, vol. 25, North-Holland Publishing Co., Amsterdam, 1979.
[26] P.-L. Lions, On the Schwarz alternating method iii: a variant for non overlapping subdomains, in: Third international Symposium on Domain Decomposition Methods for Partial Differential Equations, 1989.
[27] J. Lysmer, R.L. Kuhlemeyer, Finite dynamic model for infinite media, J. Eng. Mech. Div. 95 (1969) 859–877.
[28] V. Mattesi, M. Darbas, C. Geuzaine, A high-order absorbing boundary condition for 2D time-harmonic elastodynamic scattering problems, Comput. Math. Appl. 77 (2018) 1703–1721.
[29] A. Modave, C. Geuzaine, X. Antoine, Corner treatment for high-order local absorbing boundary conditions in high-frequency acoustic scattering, Preprint https://hal.archives-ouvertes.fr/hal-01925160, November 2018.
[30] J.-C. Nédélec, Acoustic and Electromagnetic Equations, Applied Mathematical Sciences, vol. 144, Springer, 2001.
[31] Y. Saad, M.H. Schultz, GMRES: a generalized minimal residual algorithm for solving nonsymmetric linear systems, SIAM J. Sci. Stat. Comput. 7 (3) (July 1986) 856–869.
[32] M.E. Taylor, Pseudodifferential Operators, 1981.
[33] J. Virieux, H. Calandra, R.E. Plessix, A review of the spectral, pseudo-spectral, finite-difference and finite-element modelling techniques for geophysical imaging, Geophys. Prospect. 59 (5) (2011) 794–813.
[34] K. Virta, D. Appelö, Formulae and software for particular solutions to the elastic wave equation in curved geometries, Int. J. Numer. Anal. Methods Geomech. 00 (2016) 1–19.